Sources and transformation of mercury in a karst lake ecosystem: a new perspective based on stable mercury isotopes

Hui Zhang[a], Xuewu Fu[a,*], Xian Wu[a], Qianwen Deng[a,b], Kaihui Tang[a,b], Leiming Zhang[c], Jonas Olof Sommar[a], Xinbin Feng[a,b]

[a] State Key Laboratory of Environmental Geochemistry, Institute of Geochemistry, Chinese Academy of Sciences, Guiyang, 550081, China

[b] University of Chinese Academy of Sciences, Beijing, 100049, China

[c] Air Quality Research Division, Science and Technology Branch, Environment and Climate Change Canada, Toronto, Ontario, M3H5T4, Canada

**** Corresponding Authors***

E-mail addresses: fuxuewu@mail.gyig.ac.cn (Xuewu Fu)

Abstract

Identification of sources and transformation mechanisms of mercury (Hg) is fundamental to our understanding of the biogeochemical cycling of Hg in lake ecosystems. In this study, we conducted a comprehensive investigation on the isotopic compositions of Hg in water columns, sediments, atmospheric deposition endmembers, watershed river and runoff in Hongfeng Lake (HFL) ecosystem in southwestern China. We observed significant difference in δ^{202}Hg between dissolved Hg (DHg) and particulate Hg (PHg) in lake, river, and runoff samples, with lighter isotopes preferentially adsorbed onto particulate matter. Δ^{199}Hg was also significantly higher for DHg than PHg in lake and river waters, primarily due to the higher susceptibility of DHg to photochemical reduction processes. Δ^{199}Hg and Δ^{200}Hg of Hg in sediments were similar to those of PHg in water column, but significantly different from those of DHg, reflecting the dominant role of sedimentation of PHg from water column in the Hg accumulation in sediments. The isotopic compositions of Hg in lake water and sediments lied between those of atmospheric deposition and watershed runoff end-members. Using a Hg isotope mass balance model, we estimated that runoff input accounted for 72.3% of total Hg input into the HFL ecosystem, followed by riverine input (10.3%), particulate-bound Hg (PBM) dry deposition (5.5%), Hg(II) wet deposition (5.5%), Hg(0) dry deposition (4.2%), and gaseous oxidized Hg (GOM) dry deposition (2.2%). These results highlight the key role of watershed runoff as a source of Hg in lake ecosystems and improve our understanding of the biogeochemical cycling of Hg such ecosystems.

Graphic Abstract

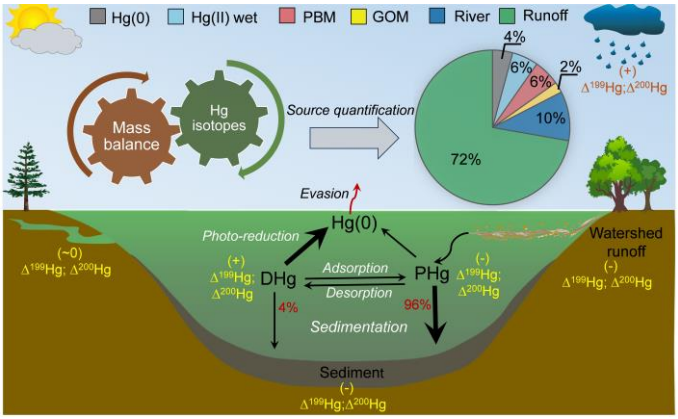

Keywords

lake ecosystem, mercury isotope fractionation, transformation process, isotope mass balance model, source apportionment

1. Introduction

Mercury (Hg) contamination in lake ecosystems is of particular concern for the environment and human health as inorganic Hg(II) entering aquatic ecosystems can be methylated by microorganisms and subsequently bioaccumulated in food chain (Blanchfield et al. 2022, Lindqvist et al. 1991). Atmospheric Hg can enter into lake waters directly through atmospheric deposition or indirectly via watersheds, where it is transported through riverine flows and surface runoff, ultimately accumulating in sediments (Cooke et al. 2020, Engstrom 2007). Despite progresses in identifying Hg sources, challenges persist in accurately quantifying the contributions from various pathways, including atmospheric wet and dry deposition, riverine transport, and surface runoff. Specifically, estimating runoff Hg and dry deposition of Hg(II), the latter one including particulate-bound Hg (PBM) and gaseous oxidized Hg (GOM), is complicated by the intricate hydrological processes governing lake-watershed interactions and uncertainties in key model parameters, such as the dry deposition velocities (V_d) of atmospheric Hg species (Jeremiason et al. 2009, Lindberg et al. 2007, Zhang et al. 2009). These knowledge gaps impede a comprehensive understanding of Hg biogeochemical cycling and the development of effective strategies for Hg pollution mitigation in lake ecosystems (Jonsson et al. 2017, Schartup et al. 2015).

The application of Hg-stable isotopes in tracing the sources and biogeochemical processes of Hg in natural ecosystems has significantly increased in recent years (Blum et al. 2014, Kwon et al. 2020, Tsui et al. 2020). The isotopic composition of Hg exhibits mass-dependent fractionation (MDF, characterized by δ^{202}Hg signatures) during most biogeochemical transport and transformation processes. Additionally, odd-mass isotopes of Hg undergo mass-independent fractionation (odd-MIF), measured as Δ^{199}Hg and Δ^{201}Hg, predominantly during photochemical reactions (Bergquist and Blum 2007, Motta et al. 2020, Sherman et al. 2010, Zheng and Hintelmann 2010). Furthermore, Even-MIF (Δ^{200}Hg and Δ^{204}Hg) is produced under specific conditions, such as the dissociation of molecular Hg(II) species at high altitudes (Chen et al. 2012, Fu et al. 2021, Sun et al. 2022). These MDF and MIF signatures provide a powerful tool for tracing Hg sources and cycling within environmental compartments, facilitating Hg source identifications in aquatic ecosystems(Blum et al. 2014, Kwon et al. 2020, Tsui et al. 2020). Despite this progress, limited information exists regarding isotopic signatures of Hg species across water profile layers and the associated

geochemical processes. Notably, the magnitude and direction of odd-MIF during liquid-phase photoreduction are influenced by the Hg(II) binding state and chemical solution properties, such as pH and dissolved oxygen (DO) concentrations (Bergquist and Blum 2007, Zheng and Hintelmann 2009, 2010). Motta et al. demonstrated that sulfhydryl-bound Hg(II) in both anaerobic and aerobic waters could induce odd-MIF, producing opposite Δ^{199}Hg signatures under photochemical conditions (Motta et al. 2020). However, this critical finding has yet to be verified through measurements on natural surfaces. Most existing previous studies have focused on the Hg sources in sediments using isotopic techniques. For instance, Chen et al. (2016) observed different Hg isotopic compositions between dissolved Hg (DHg) and sediment Hg, suggesting that Hg in lake sediments have different sources from DHg (Chen et al. 2016); however, the sources of Hg to lake sediments and waters were not quantified mainly due to the lack of Hg isotopes observations of the other Hg species (e.g., particulate Hg (PHg)) in water and external loading sources (atmospheric deposition, riverine input, and watershed runoff). Similarly, Lepak et al. (2015, 2020) investigated the contributions of watersheds, precipitation, and industrial sources to Hg in Great Lakes sediments, but did not consider the contributions from atmospheric Hg (Hg(0), PBM, and GOM) dry deposition and riverine input (Lepak et al. 2020, Lepak et al. 2015). The Hg isotopic signatures of lake waters across vertical profiles, which serve as critical links between input sources and sediments, remain poorly understood.

In this study, we measured Hg concentrations and isotopic compositions across multiple environmental compartments in the Hongfeng Lake (HFL) ecosystem, located in southwestern China. Sampling included atmospheric PBM, precipitation, river water, surface runoff, lake water, and sediments. These measurements were integrated with previously reported data on Hg isotope fractionation during air-water exchange of Hg(0) to delineate the Hg sources in the HFL ecosystem (Zhang et al. 2023). Based on the comprehensive observations of Hg concentration and isotopes and using a novel Hg isotope mass balance model, we have unraveled the transformation mechanisms (e.g., conversion, photochemical reduction, and sedimentation) of DHg and PHg in waters and quantified the contributions of atmospheric Hg deposition (Hg(0), PBM, GOM dry deposition and Hg(II) wet deposition), riverine input, and watershed runoff to Hg in the lake ecosystem.

2. Materials and methods

2.1. Site description and sample processing

Hongfeng Lake (HFL, 26°25′N~26°34′N, 106°20′~106°26′E), located in the Yunnan-Guizhou Plateau of southwestern China, is the region's largest karst lake and serves as a vital drinking water source for Guiyang City. HFL consists of two primary basins: the northern and the southern lake basin. Its hydrology is largely sustained by direct rainfall and inflows from four main tributaries: the Maiweng, Yangchang, Maxian, and Houliu Rivers, with the Maotiao River acting as the lake's sole outlet (Fig. 1). Comprehensive hydrological and water quality data are provided in the Supporting Information (Text S1, Fig. S1, Table S1).

PBM samples were collected onto preheated (500 °C for 6 h) quartz filters (Munktell) using a high-volume mass flow-controlled system for $PM_{2.5}$ sampling (ASM-1, China) from January to October 2020 at the HFL ecological observatory (Fig. 1). Each sampling event lasted 72 hours with a volumetric flow rate of 1.0 m^3 min^{-1}. Immediately following collection, the quartz filters were carefully sealed in polypropylene bags to prevent contamination prior to laboratory processing. For Hg isotope analysis, samples were preconcentrated into 5 mL of a 40% HNO_3/HCl mixed acid solution (v/v, 2:1) using a double-stage combustion method, following the procedure detailed in a previous study (Huang et al. 2015).

Precipitation samples were collected using an automated deposition collector (APS-3A, China, details in Text S2) from March to October 2020. River water samples were obtained from the four major upstream rivers and the single downstream river using clean acrylic water samples in March and July 2020. Runoff samples were collected from the northern and southern catchments of HFL with a Teflon runoff collector from May to July 2020 (Fig. 1) (Xia et al. 2021). Monthly samples of precipitation, river water, and runoff were obtained. Lake water samples were taken from various depths in the northern and southern basins of HFL using a Niskin water sampler (Watertools, China) during the spring, summer, and winter of 2020. All collected water samples (river, runoff, and lake water) were immediately filtered on-situ to analyze DHg and PHg using a pre-cleaned aspirator with treated quartz filter (Whatman, 2.2μm pore size). The filtered water was subsequently acidified with 5‰ (v/v) trace-metal reagent grade HCl and digested overnight (12 h) with 3 ‰ (v/v) BrCl (0.2 mol/L) in 10 L brown borosilicate glass bottles, and then stored at 4℃ in the laboratory for subsequent preconcentration for Hg isotope analysis (EPA 2002, Li et al. 2019, Zhang et al. 2021).

For DHg analysis, samples were collected preconcentrated using chlorine-impregnated activated carbon (CLC) traps, following a procedure detailed in (Zhang et al. 2021), and then concentrated into 5 mL of 40% mixed acid solution. For PHg, filter samples were freeze-dried and then preconcentrated in 5 mL of 40% mixed acid solution using a two-stage furnace system for isotope analysis(Jiskra et al. 2021).

Sediment cores and surface sediment were collected from the northern basin of HFL in January 2021. Sediment cores were obtained using a gravity coring system, sliced, and stored in polypropylene centrifuge tubes for subsequent analysis. In the laboratory, these sediment samples were freeze-dried, weighed, and sieved to determine Hg concentration, isotopic composition, and age. The sediment cores were dated using excess ^{210}Pb, analyzed with a multi-channel γ-ray spectrometer (GX6020, Canberra, USA). The chronologies of sediment core was calculated through the constant flux and constant sedimentation rate model to derive the sedimentation flux of Hg (Text S3) (Appleby and Oldfield 1978). Surface sediment samples were collected with a Peterson sampler and preconcentrated by combustion in a two-stage furnace system for Hg isotope analysis (Sun et al. 2013).

2.2. Hg concentration and stable isotope analysis

Hg concentrations in acid trapping solution were determined by cold vapor atomic fluorescence spectrometry (CVAFS) according to the EPA 1631 protocol (EPA 2002). Hg concentrations in particulate matter and sediment were determined by a DMA-80 automated mercury analyzer. Hg isotope ratios were determined at the State Key Laboratory of Environmental Geochemistry, CAS, (Guiyang, China) using a Nu-Plasma II MC-ICPMS following the analytical procedures described by Blum and Bergquist (Blum and Bergquist 2007). The isotopic ratios were corrected for mass bias by standard bracketing of samples using NIST 3133 (Blum and Bergquist 2007). MDF, expressed as the delta notation (δ, reported in ‰), is relative to the NIST3133 standard reference value and is calculated as follows (Blum and Bergquist 2007):

$$\delta^{xxx}Hg(‰) = \left[\frac{(^{xxx}Hg/^{198}Hg)_{Sample}}{(^{xxx}Hg/^{198}Hg)_{SRM\ 3133}} - 1\right] \times 10^3‰ \quad (1)$$

where *xxx* is the mass number of each Hg isotopes between 199 and 204. MIF is expressed as the capital delta notation (Δ) and is defined as the difference between the measured δ^{xxx}Hg and the theoretically predicted δ^{xxx}Hg using the kinetic MDF law (Blum and Bergquist 2007):

$$\Delta^{xxx}Hg(‰) = \delta^{xxx}Hg - \beta^{xxx} \times \delta^{202}Hg \quad (2)$$

where β^{xxx} is the scaling factor determined by the kinetic mass-dependent law and has values of 0.2520, 0.5024, 0.7520, and 1.493 for the masses of Hg isotopes 199, 200, 201, and 204, respectively (Blum and Bergquist 2007).

Standard quality assurance and control procedures were strictly followed during the analysis of Hg, as outlined in Text S4. Analytical precision (± 2SD) was evaluated by conducting repeated measurements of the secondary standards NIST SRM 3177 and RM 8610 during each isotope analysis. Additionally, the Hg isotopic compositions of certified reference materials (CRMs) BCR 482 (Lichen) and SRM 1947 (Fish) were measured, with all results aligning well with previously reported values (Table S2) (Blum and Johnson 2017, Blum et al. 2014).

2.3. Hg isotope mass balance model for source apportionment

All the potential pathways for Hg inflow and outflow within the HFL ecosystem were integrated into the Hg isotope mass balance model. The inflow pathways include Hg wet deposition, atmospheric GOM, PBM, and Hg(0) dry deposition, runoff, and riverine input. The outflow pathways comprise Hg(0) evasion from water, Hg sedimentation, and export of Hg through the downstream river and municipal water supply systems. Given the relatively short residence time of Hg in the lake (~36 days), the Hg system in HFL is presumed to attain a steady-state equilibrium between input and output shortly after the loading of Hg from various sources to the lake (Gao et al. 2006, Vette et al. 2002). It is therefore assumed that the mass of Hg within the water column remains constant, with the imported Hg fluxes and their respective isotopic signatures balanced by the Hg export fluxes. Atmospheric GOM and PBM dry deposition, riverine and runoff Hg input, which are unknown or difficult to be quantified, are needed to further considered in the Hg isotope mass balance model, as detailed in Table S1 and Text S5. As a result, the contributions of various sources to the HFL can be determined using the following equation, with all variables expressed on annual basis:

$$M_{Hg(0)-Dep} + M_{Wet} + M_{PBM} + M_{GOM} + M_{River} + M_{Runoff} = M_{Sed} + M_{Out} + M_{Hg(0)-Eva} \quad (3)$$

$$M_{Hg(0)-Dep} \times \delta^{202}Hg_{Hg(0)-Dep} + M_{Wet} \times \delta^{202}Hg_{Wet} + M_{PBM} \times \delta^{202}Hg_{PBM} + M_{GOM} \times \delta^{202}Hg_{GOM} + M_{River} \times \delta^{202}Hg_{River} + M_{Runoff} \times \delta^{202}Hg_{Runoff} = M_{Sed} \times \delta^{202}Hg_{Sed} + M_{Out} \times \delta^{202}Hg_{Lake} + M_{Hg(0)-Eva} \times \delta^{202}Hg_{Hg(0)-Eva} \quad (4)$$

$$M_{Hg(0)-Dep} \times \Delta^{199}Hg_{Hg(0)-Dep} + M_{Wet} \times \Delta^{199}Hg_{Wet} + M_{PBM} \times \Delta^{199}Hg_{PBM} + M_{GOM} \times \Delta^{199}Hg_{GOM} + M_{River} \times \Delta^{199}Hg_{River} + M_{Runoff} \times \Delta^{199}Hg_{Runoff} = M_{Sed} \times \Delta^{199}Hg_{Sed} + M_{Out} \times \Delta^{199}Hg_{Lake} + M_{Hg(0)-Eva} \times \Delta^{199}Hg_{Hg(0)-Eva} \quad (5)$$

$$M_{Hg(0)-Dep} \times \Delta^{200}Hg_{Hg(0)-Dep} + M_{Wet} \times \Delta^{200}Hg_{Wet} + M_{PBM} \times \Delta^{200}Hg_{PBM} + M_{GOM} \times \Delta^{200}Hg_{GOM} + M_{River} \times \Delta^{200}Hg_{River} + M_{Runoff} \times \Delta^{200}Hg_{Runoff} = M_{Sed} \times \Delta^{200}Hg_{Sed} + M_{Out} \times \Delta^{200}Hg_{Lake} + M_{Hg(0)-eva} \times \Delta^{200}Hg_{Hg(0)-Eva} \quad (6)$$

In the model, $M_{Hg(0)\text{-}Dep}$, M_{PBM}, and M_{GOM} represent dry deposition fluxes of atmospheric Hg(0), PBM, and GOM, respectively, while M_{Wet} denotes Hg wet deposition. Riverine and runoff input are represented by M_{River} and M_{Runoff}, respectively. The fluxes of Hg sedimentation, export, and evasion from the lake are denoted by M_{Sed}, M_{Out}, and $M_{Hg(0)\text{-}Eva}$, respectively. Furthermore, $\delta^{202}Hg_{yyy}$, $\Delta^{199}Hg_{yyy}$, and $\Delta^{200}Hg_{yyy}$ represent the Hg isotopic signatures in various environmental media, with "yyy" corresponding to the following: "Dep" for Hg(0) deposition to water, "PBM" for atmospheric PBM, "GOM" for atmospheric GOM, "wet" for precipitation Hg(II), "river", "runoff", and "lake" for water Hg in these respective media, "Sed" for sediment Hg(II), and "Hg(0)-Eva" for Hg(0) evasion from water. The isotopic compositions of GOM, water Hg(0) evasion, and Hg(0) deposited are sourced from previous studies (Rolison et al. 2013, Zhang et al. 2023). Monte Carlo simulations were performed using R code to estimate the uncertainties associated with the Hg isotope mass balance model.

3. Results and discussion

3.1 Hg concentrations and isotopic compositions of end-member sources

The mean (±1SD) concentrations of DHg and PHg in precipitation samples were 8.82 ± 2.26 ng/L (n = 17) and 10.92 ± 7.17 ng/L (n = 15, Fig. S2 and Table S3), respectively. The mean (±1SD) concentrations of atmospheric PBM was 52.1 ± 4.6 pg/m^3 (n = 16, Table S4), which was slightly higher than values observed at other remote sites (40.0 ± 47.9 pg/m^3, n = 11, 1SD), but significantly lower than concentrations recorded at urban locations in China (238.3 ± 133.4 pg/m^3, n = 8, 1SD) (Feng et al. 2022, Zhang et al. 2022).

Mean (±1SD) concentrations of DHg and PHg in river waters were 4.03 ± 1.18 ng/L (n = 10) and 9.08 ± 2.86 ng/L (n = 10), respectively (Table S5). These concentrations were approximately 4 and 8 times lower than the corresponding mean concentrations of DHg (14.83 ± 3.03 ng/L, n = 6)

and PHg (73.56 ± 34.69 ng/L, n = 13) in runoff samples (Table S6). The Hg concentrations of runoff were generally consistent with those previously reported for karst catchments (Xia et al. 2021) and forested watersheds (Jiskra et al. 2017).

The isotopic compositions of PBM and precipitation Hg(II) were characterized by similar negative δ^{202}Hg (median: -1.41‰ and -1.15‰; interquartile range (IQR), -1.85 to -1.20‰ and -1.22 to -1.03‰; n = 16 and 12, respectively), as well as positive Δ^{199}Hg (median: 0.23‰ and 0.21‰; IQR: 0.19 to 0.29‰ and 0.17 to 0.25‰, respectively) and Δ^{200}Hg values (median: 0.07‰ and 0.09‰; IQR: 0.05 to 0.12‰ and 0.07 to 0.10‰, respectively) (Fig. 2 and S2, Table S3 and S4). These isotopic signatures of PBM and precipitation Hg(II) were consistent with those reported for remote areas globally (Fu et al. 2021, Kwon et al. 2020, Washburn et al. 2021).

The isotopic compositions of DHg in river water exhibited a negative median δ^{202}Hg of -1.02‰ (IQR: -1.09 to -1.01‰), alongside positive median Δ^{199}Hg of 0.17‰ (IQR: 0.16 to 0.18‰) and Δ^{200}Hg of 0.08‰ (IQR: 0.07 to 0.11‰). For PHg in river water, the isotopic signatures were relatively lower, with the median values of δ^{202}Hg of -1.69‰ (IQR: -1.79 to -1.51‰), Δ^{199}Hg of -0.06‰ (IQR: -0.07 to -0.05‰), and Δ^{200}Hg of 0.00‰ (IQR: 0.00 to 0.01‰) (Figure 2, Table S5). In runoff, the median δ^{202}Hg of PHg was more negative than that of DHg (-1.69‰ vs. -1.06‰, respectively), with this difference between the two being similar to that observed in river water. However, DHg and PHg in runoff had similar negative Δ^{199}Hg (median: -0.10‰, IQR: -0.12 to -0.08‰ and median: -0.13‰, IQR: -0.14 to -0.11‰, respectively) and Δ^{200}Hg (median: -0.05‰, IQR: -0.05 to -0.04‰ and median: -0.04‰, IQR: -0.05 to -0.04‰, respectively) (Fig. 2, Table S6). The Δ^{199}Hg and Δ^{200}Hg signatures of DHg and PHg in runoff were similar to those of foliage Hg in this study area (median Δ^{199}Hg: -0.29‰, IQR: -0.34 to -0.09‰; median Δ^{200}Hg: -0.04‰, IQR: -0.05 to -0.04‰, Table S7). Given that soil-bound Hg associated with natural organic matter (NOM) primarily originates from the decomposition of litterfall (Demers et al. 2013, Jiskra et al. 2015, Wang et al. 2017), it is likely that the dominant source of Hg in runoff is soil leaching of NOM-bound Hg, which itself is derived from foliage uptake of atmospheric Hg(0). This implies that precipitation-derived Hg(II) plays a minor role in contributing to runoff Hg. Such findings align with studies from forested watersheds in northern Sweden, where precipitation Hg(II) was found to contribute minimally to runoff Hg (Jiskra et al. 2017).

3.2. Variations of Hg concentration and isotope composition in lake water column

The mean (± 1SD) concentrations of DHg in the HFL water column were 1.15 ± 0.43 ng/L (n = 20), 1.74 ± 0.56 ng/L (n = 18), and 1.60 ± 0.55 ng/L (n = 22) (Table S8), and those of PHg were 3.12 ± 0.59 ng/L (n = 20), 3.08 ± 1.00 ng/L (n = 18), and 2.69 ± 0.60 ng/L (n = 22) (Table S9) in winter, spring, and summer, respectively. In terms of vertical distribution, both DHg and PHg concentrations in HFL exhibited a marked decline with increasing depth (Fig. 3). We hypothesize that the observed pattern in HFL is driven primarily by specific physicochemical factors within the water column, such as sulfate levels, dissolved iron, dissolved organic carbon (DOC)), and suspended particulate matter (SPM). Furthermore, auxiliary water chemistry in the northern and southern basins of HFL also shows a decrease with increasing depth (Fig. S1). Additionally, significant positive correlations between DHg and DOC concentrations, as well as between PHg and SPM, were observed across all sampling events (Fig. S3), indicating that organic matter and suspended particles exert a significant control on vertical transport of Hg within lake water column.

The isotopic compositions of DHg in lake water samples revealed a negative median δ^{202}Hg of -0.85‰ (IQR: -1.08 to -0.65‰) and positive median Δ^{199}Hg and Δ^{200}Hg of 0.17‰ (IQR: 0.13 to 0.24‰) and 0.03‰ (IQR: 0.01 to 0.06‰), respectively. In contrast, PHg exhibited lower isotopic values than DHg, with median δ^{202}Hg, Δ^{199}Hg, and Δ^{200}Hg values of -1.53‰ (IQR: -1.74 to -1.34‰), -0.04‰ (IQR: -0.07 to -0.02‰), and -0.01‰ (IQR: -0.03 to 0.00‰), respectively, (Fig. 2). Unlike the concentration trends of DHg and PHg, the isotopic signatures, particularly Δ^{199}Hg and Δ^{200}Hg, did not exhibit distinct vertical distribution patterns in the water column (Fig. 3, Table S8 and S9). The insignificant variation of δ^{202}Hg with depth indicates the influence of complicated biogeochemical processes (Tsui et al. 2020). In lake surface water, the Hg(II) photochemical reaction in the presence of DOC leads to higher Δ^{199}Hg (Zhang et al. 2023); however, the intensity of this reaction decreases significantly with reduced light availability (Motta et al. 2020). Given the transparency of only 2m in the HFL, it is expected that the Δ^{199}Hg signal in surface water would exhibit a significantly positive value, which would distinguish it from deeper water layers. However, vertical mixing likely facilitated sufficient mixing between surface and deeper waters, which may explain the absence of a clear vertical distribution trend for Δ^{199}Hg. Additionally, remobilization of Hg from sediments and groundwater inputs, which typically display negative odd-MIF

characteristics, likely exerts minimal influence on the vertical trend of Hg Δ^{199}Hg in the water column (Table S10).

3.3. Hg sedimentation flux and sediment Hg isotopic compositions

The mean (± 1SD) concentration of Hg in surface sediment was 474.2 ± 27.9 ng/g (n = 7, Table S10). We calculated the annual flux of THg from the water column to the sediment, referred to as sedimentation loss below, using sediment Hg concentration (ng/g), mass depth (g/cm^2), and sediment age (a), as detailed in Text S3 and Table S1. The calculated sedimentation loss was 0.85 μg/m^2/yr, integrating which over the whole lake gives a value of 27.54 ± 1.85 kg/yr, accounting for 81% of the total loss of Hg from the lake water (Table S1). Such a finding with the major loss of Hg being from sedimentation processes is consistent with that reported for Lake Superior and Lake Michigan (Jeremiason et al. 2009), but differs from that reported for Lake Champlain where volatilization of Hg(0) from the water body was the largest loss (Gao et al. 2006). The disparate outcomes with respect to the predominant losses between these lakes are plausibly attributable to their disparate PHg fractions relative to THg in the water column and residence times of Hg in lakes. For instance, HFL has a PHg/THg ratio of approximately 1:1.5, with a residence time of Hg at 36 days, whereas Lake Champlain has a much lower PHg/THg ratio of 1:23.7 and a residence time closed to a year.

Hg in surface sediment in HFL had negative median δ^{202}Hg, Δ^{199}Hg, and Δ^{200}Hg values of -1.65‰ (IQR: -1.72 to -1.56‰, n = 7), -0.08‰ (IQR: -0.09 to -0.07‰), and -0.04‰ (IQR: -0.04 to -0.03‰), respectively (Fig. 2, Table S10). These isotopic compositions are consistent with those previously reported for sediments in remote regions, where median (± 1SD) values of δ^{202}Hg, Δ^{199}Hg, and Δ^{200}Hg were -1.34 ± 0.30‰, -0.19 ± 0.08‰ and -0.02 ± 0.02‰, respectively (Fig. 2) (Guédron et al. 2016, Lee et al. 2021, Lepak et al. 2020). A notable feature of these sediments with negative Δ^{199}Hg and Δ^{200}Hg signatures is their high watershed to lake area ratios, which range from 8.2 to 15.1, with HFL showing a ratio of 28. Such ratios indicate that the majority of Hg in these lakes is derived from the watershed, which is in contrast to sediments from lakes with smaller watershed to lake area ratios, typically associated with positive Δ^{199}Hg and Δ^{200}Hg values (Kurz et al. 2019, Lee et al. 2021).

3.4 Transformation of Hg in lake water column

Our observations showed that DHg and PHg in HFL water column are characterized by distinct isotopic values. We observed a notable positive shift in δ^{202}Hg for DHg relative to PHg in lake water, a pattern that is similar to those for river water and watershed runoff (Fig. 4). The median shift, defined as D-$\delta^{202}Hg_{DHg-PHg}$ = $\delta^{202}Hg_{DHg}$-$\delta^{202}Hg_{PHg}$, was approximately 0.69‰, 0.65‰, and 0.63‰ for lake water, river water, and runoff, respectively. These values are comparable to previously observed shifts in river and sea water, with D-$\delta^{202}Hg_{DHg-PHg}$ of 0.40‰ and 0.75‰, respectively (Campeau et al. 2022, Jiskra et al. 2021). The positive shift of δ^{202}Hg in DHg relative to PHg is consistent with the MDF trajectories documented during the photochemical/abiotic dark/microbial reduction of Hg(II) by DOC and the Hg(II) adsorption/desorption experiments (Bergquist and Blum 2007, Jiskra et al. 2012, Tsui et al. 2020, Wiederhold et al. 2010, Zheng and Hintelmann 2009), suggesting that isotopic differentiation between DHg and PHg is likely driven by reduction of Hg(II) by DOC and/or Hg(II) adsorption/desorption processes.

DHg in lake and river waters had much higher Δ^{199}Hg and Δ^{200}Hg values than those of PHg (Fig. 4), consistent with previous studies in seawater and river water (Campeau et al. 2022, Jiskra et al. 2021). Such a notable difference in Hg-MIF indicates a slow transformation between DHg and PHg species in lake and river waters, otherwise we would expect similar Hg-MIF signatures between DHg and PHg. Our observation raises the question of what underlying processes are responsible for the higher Δ^{199}Hg signatures observed in DHg in lake and river waters. A scatter plot of Δ^{199}Hg vs. Δ^{200}Hg for DHg and PHg revealed that the majority of DHg data points were positioned above the mixing line, while PHg points were evenly distributed on both sides of the line representing the typical atmospheric Hg(0) and atmospheric Hg(II) source end-members (Fig. S4). The positive shift of Δ^{199}Hg in DHg, as compared to what would be expected from atmospheric source mixing, suggests that post-depositional processes have shifted the Δ^{199}Hg signatures of DHg. The linear regression of Δ^{199}Hg vs. Δ^{201}Hg for DHg in lake and river waters yielded a slope of 1.09 ± 0.01 (Fig. S5), indicating photochemical reduction induced Hg MIF. The observed more positive Δ^{199}Hg in water DHg as compared to the mixing of atmosphere end-members seems to be in line with the fractionation trajectories of photochemical reduction of Hg(II) in presence of DOC, a process that has resulted in more positive Δ^{199}Hg in residual DHg (Zhang et al. 2023). In contrast, PHg appears to be relatively stable against photochemical reduction, resulting in a Δ^{199}Hg signature

that aligns more closely with atmospheric mixing sources. These findings are overall consistent with previous experimental studies, which have suggested photochemical reduction processes should be mainly associated with dissolved or colloidal Hg(II) (Amyot et al. 1997, Ci et al. 2016). We further compared the previously measured Δ^{200}Hg values of Hg(0) emissions from water in HFL, which is mainly driven by Hg(II) photochemical reduction (Zhang et al. 2023), with those of DHg and PHg (Fig. S6). The Δ^{200}Hg signature of water Hg(0) emissions closely aligned with that of DHg, but diverged significantly from that of PHg (Paired *t*-test, $p < 0.01$), indicating that DHg, rather than PHg, is the primary Hg species involved in photochemical reduction. The minimal contribution of PHg to water Hg(0) emissions reinforces the hypothesis that DHg is more susceptible to photochemical reduction, which accounts for the higher Δ^{199}Hg values observed in DHg in both lake and river waters.

Accumulation of Hg in sediment is thought to be dominated by sedimentation of particulate matter, but could be also affected by the exchange of dissolved Hg(II) between sediment-water interface (Ullrich et al. 2001). The sedimentation of PHg and DHg and their relative contributions to sediments Hg are, however, not well constrained. Here we found sediment Hg in HFL had negative Δ^{199}Hg and Δ^{200}Hg values (median: -0.08‰ and -0.04‰, respectively), a signature closely aligned with those of PHg in water column but statistically lower than those of DHg ($p < 0.001$, ANOVA test, Fig. 4). The difference in Δ^{199}Hg and Δ^{200}Hg between sediment and DHg are not likely caused by diffusion and/or adsorption-desorption processes, which is thought to produce negligible odd-MIF and even-MIF(Jiskra et al. 2012, Wiederhold et al. 2010). We therefore proposed that accumulation of Hg in HFL sediments should be mainly derived from the sedimentation of PHg in water column. Based on a Δ^{199}Hg isotope mass balance model (Text S6), we estimate that approximately 95.8 ± 2.0% of sediment Hg is derived from PHg sedimentation, which significantly outweighs the contribution from lake DHg (4.2 ± 2.0%). This finding underscores the importance of the sedimentation of PHg, rather than DHg, from the water column as the primary source of Hg in sediments. This, together with the stable nature of PHg against photochemical reduction as discussed earlier, indicate that the variations of Hg-MIF in sediments in lakes like HFL are more likely related to the changes of loading sources.

3.5. Comprehensive quantification of Hg sources in HFL ecosystem

In this study, a source apportionment analysis of Hg in the HFL ecosystem was carried out by integrating estimated fluxes from various Hg sources and sinks with source-specific isotopic compositions, utilizing a combined Hg mass balance and isotope mass balance model (Section 2.4, Table S1, Text S5). The Hg input fluxes from direct atmospheric Hg(0), PBM, and GOM dry deposition, Hg wet deposition, riverine, and runoff input were estimated to be 1.43 ± 0.37, 1.87 ± 1.57, 0.76 ± 0.65, 1.87 ± 0.67, 3.51 ± 2.66, and 24.62 ± 2.55 kg/yr (mean ± 1SD), respectively, within the HFL ecosystem (Fig. 5). Apparently, the largest contribution to Hg in the HFL ecosystem was from runoff (72.3%), followed by the riverine input (10.3%), atmospheric PBM dry deposition (5.5%), wet deposition (5.5%), atmospheric Hg(0) dry deposition (4.2%), and GOM dry deposition (2.2%) (Fig. 5). The elevated Hg concentrations observed in runoff highlight its significant role as the dominant source of Hg inputs. While previous studies have emphasized the critical importance of watershed-derived Hg (Cooke et al. 2020, Lepak et al. 2020, Lepak et al. 2015, Swain et al. 1992), this study is unique in quantifying the contributions of Hg from watershed sources and distinguishing the relative roles of riverine versus surface runoff inputs, an analysis that has not been explored in prior research. Atmospheric Hg(0) enters the lake ecosystem primarily through two pathways: direct deposition onto the lake surface and uptake by vegetation followed by transport through watershed runoff. Our findings underscore the importance of watershed runoff as a major pathway for Hg accumulation in the HFL lake ecosystem, with contributions from runoff exceeding those from direct atmospheric Hg(0) deposition to surface waters.

Atmospheric Hg deposition encompasses Hg(0), PBM, and GOM, each playing critical roles in Hg cycling. Our previous research estimated an average Hg(0) dry deposition velocity (V_d) of 0.03 cm/s over HFL (Zhang et al. 2023). Based on the estimated annual mean PBM and GOM dry deposition fluxes and their corresponding concentrations (GOM concentrations obtained from the literature (Feng et al. 2022)), V_d values for PBM and GOM were calculated as 1.1 and 1.2 cm/s, respectively. These estimates align with previously reported values for GOM deposition over lake surfaces (0.9 ~ 5.0 cm/s; (Engle et al. 2010, Peterson and Gustin 2008)) but exceed modeled values for PBM (0.02 ~ 0.37 cm/s; (Engle et al. 2010)). The higher PBM deposition rates likely reflect contributions from coarse particles (~10 μm), as suggested by Stoke' law, necessitating further experimental verification. It is hypothesized that the observed PBM is predominantly associated

with dust, potentially derived from anthropogenic sources such as cement production, or bioaerosols.

4. Conclusions and implications

This study, based on stable Hg isotopes, provides a comprehensive investigation on the sources and transformation mechanisms of Hg within a karst lake ecosystem. Our observations reveal that lighter Hg isotopes are preferentially enriched in particle-bound Hg in rivers, runoff, and lake waters. DHg in both river and lake water had more positive Δ^{199}Hg values relative to PHg, indicating that DHg is more susceptible to photochemical reduction reactions than PHg. Furthermore, our observations show that approximately 96% of the Hg accumulated in sediments in the HFL is derived from the sedimentation of PHg from the water column, while the contribution of DHg is negligible. Based on Hg isotope mass balance model, we unravel that the loading of Hg to the HFL lake ecosystem is dominated (72.3%) by watershed runoff, supporting previous hypothesis that Hg isotopic compositions in lake sediments predominantly reflect watershed-derived sources rather than in-lake processes (Jiskra et al. 2022, Lee et al. 2021, Lepak et al. 2020). Although the specific sources of Hg may vary with different lake ecosystems, the methodological framework presented in this study provides a valuable tool for future investigations into the sources and biogeochemical cycling of Hg in aquatic systems.

The study highlights the critical role of the re-mobilization of legacy Hg, which has been deposited in watershed, in driving Hg cycling within lake ecosystems. Given the substantial Hg reservoirs in these watersheds, coupled with the ongoing influx of Hg through runoff (Liu et al. 2019, Liu et al. 2018), it is expected that the transport of Hg via erosion will continue to play a significant role in Hg dynamics in lake ecosystems. This will persist even after atmospheric Hg deposition decreases due to the implementation of the UN Minamata Convention, which aims to reduce anthropogenic Hg emissions. As Hg budgets in watersheds transiting into a phase of legacy depletion (Powers et al. 2016), the re-mobilization of Hg is anticipated to remain an ongoing process over several decades. These findings underscore the importance of adopting long-term, sustainable management strategies to address the issue of legacy Hg pollution. Such strategies, akin to those established for phosphorus management (Haygarth et al. 2014), are essential for mitigating Hg risks and safeguarding vulnerable karst ecosystems.

Acknowledgment

This work was funded by the National Nature Science Foundation of China (42394092, 42407357), and the Key Research Program of Frontier Science (ZDBS-LY-DQC029) and the Strategic Priority Research Program (XDB40020404) of Chinese Academy of Sciences.

References

1. Amyot, M., Gill, G.A. and Morel, F.M.M. (1997) Production and loss of dissolved gaseous mercury in coastal seawater. Environmental Science & Technology 31(12), 3606-3611.

2. Appleby, P.G. and Oldfield, F.R. (1978) The calculation of lead-210 dates assuming a constant rate of supply of unsupported 210 Pb to the sediment. Catena 5(1), 1-8.

3. Bergquist, B.A. and Blum, J.D. (2007) Mass-dependent and -independent fractionation of Hg isotopes by photoreduction in aquatic systems. Science 318(5849), 417-420.

4. Blanchfield, P.J., Rudd, J.W.M., Hrenchuk, L.E., Amyot, M., Babiarz, C.L., Beaty, K.G., Bodaly, R.A.D., Branfireun, B.A., Gilmour, C.C., Graydon, J.A., Hall, B.D., Harris, R.C., Heyes, A., Hintelmann, H., Hurley, J.P., Kelly, C.A., Krabbenhoft, D.P., Lindberg, S.E., Mason, R.P., Paterson, M.J., Podemski, C.L., Sandilands, K.A., Southworth, G.R., St Louis, V.L., Tate, L.S. and Tate, M.T. (2022) Experimental evidence for recovery of mercury-contaminated fish populations. Nature 601(7891), 74-+.

5. Blum, J.D. and Bergquist, B.A. (2007) Reporting of variations in the natural isotopic composition of mercury. Analytical and Bioanalytical Chemistry 388(2), 353-359.

6. Blum, J.D. and Johnson, M.W. (2017) Recent Developments in Mercury Stable Isotope Analysis. Non-Traditional Stable Isotopes 82, 733-757.

7. Blum, J.D., Sherman, L.S. and Johnson, M.W. (2014) Mercury Isotopes in Earth and Environmental Sciences. Annual Review of Earth and Planetary Sciences, Vol 42 42, 249-269.

8. Campeau, A., Eklöf, K., Soerensen, A.L., Åkerblom, S., Yuan, S.L., Hintelmann, H., Bieroza, M., Köhler, S. and Zdanowicz, C. (2022) Sources of riverine mercury across the Mackenzie River Basin; inferences from a combined Hg-C isotopes and optical properties approach. Science of the Total Environment 806, 150808.

9. Chen, J.B., Hintelmann, H., Feng, X.B. and Dimock, B. (2012) Unusual fractionation of both odd and even mercury isotopes in precipitation from Peterborough, ON, Canada. Geochimica Et Cosmochimica Acta 90, 33-46.

10. Chen, J.B., Hintelmann, H., Zheng, W., Feng, X.B., Cai, H.M., Wang, Z.H., Yuan, S.L. and Wang, Z.W. (2016) Isotopic evidence for distinct sources of mercury in lake waters and sediments. Chemical Geology 426, 33-44.

11. Ci, Z.J., Zhang, X.S., Yin, Y.G., Chen, J.S. and Wang, S.W. (2016) Mercury Redox Chemistry in Waters of the Eastern Asian Seas: From Polluted Coast to Clean Open Ocean. Environmental Science & Technology 50(5), 2371-2380.

12. Cooke, C.A., Martínez-Cortizas, A., Bindler, R. and Gustin, M.S. (2020) Environmental archives of atmospheric Hg deposition - A review. Science of the Total Environment 709, 134800.

13. Demers, J.D., Blum, J.D. and Zak, D.R. (2013) Mercury isotopes in a forested ecosystem: Implications for air-surface exchange dynamics and the global mercury cycle. Global Biogeochemical Cycles 27(1), 222-238.

14. Engle, M.A., Tate, M.T., Krabbenhoft, D.P., Schauer, J.J., Kolker, A., Shanley, J.B. and Bothner, M.H. (2010) Comparison of atmospheric mercury speciation and deposition at nine sites across central and eastern North America. Journal of Geophysical Research-Atmospheres 115.

15. Engstrom, D.R. (2007) Fish respond when the mercury rises. Proceedings of the National Academy of Sciences of the United States of America 104(42), 16394-16395.

16. EPA, U., Method 1631, Revision E: (2002) Mercury in water by oxidation, purge and trap, and cold vapor atomic fluorescence spectrometry (EPA, 2002). United States Environmental Protection

Agency, Washington, DC, , 1-33.

17. Feng, X.B., Li, P., Fu, X.W., Wang, X., Zhang, H. and Lin, C.J. (2022) Mercury pollution in China: implications on the implementation of the Minamata Convention. Environmental Science-Processes & Impacts 24(5), 634-648.

18. Fu, X.W., Jiskra, M., Yang, X., Marusczak, N., Enrico, M., Chmeleff, J., Heimburger-Boavida, L.E., Gheusi, F. and Sonke, J.E. (2021) Mass-Independent Fractionation of Even and Odd Mercury Isotopes during Atmospheric Mercury Redox Reactions. Environmental Science & Technology 55(14), 10164-10174.

19. Gao, N., Armatas, N.G., Shanley, J.B., Kamman, N.C., Miller, E.K., Keeler, G.J., Scherbatskoy, T., Holsen, T.M., Young, T., McIlroy, L., Drake, S., Olsen, B. and Cady, C. (2006) Mass balance assessment for mercury in Lake Champlain. Environmental Science & Technology 40(1), 82-89.

20. Guédron, S., Amouroux, D., Sabatier, P., Desplanquee, C., Develle, A.L., Barre, J., Feng, C.Y., Guiter, F., Arnaud, F., Reyss, J.L. and Charlet, L. (2016) A hundred year record of industrial and urban development in French Alps combining Hg accumulation rates and isotope composition in sediment archives from Lake Luitel. Chemical Geology 431, 10-19.

21. Haygarth, P.M., Jarvie, H.P., Powers, S.M., Sharpley, A.N., Elser, J.J., Shen, J.B., Peterson, H.M., Chan, N.I., Howden, N.J.K., Burt, T., Worrall, F., Zhang, F.S. and Liu, X.J. (2014) Sustainable Phosphorus Management and the Need for a Long-Term Perspective: The Legacy Hypothesis. Environmental Science & Technology 48(15), 8417-8419.

22. Huang, Q., Liu, Y.L., Chen, J.B., Feng, X.B., Huang, W.L., Yuan, S.L., Cai, H.M. and Fu, X.W. (2015) An improved dual-stage protocol to pre-concentrate mercury from airborne particles for precise isotopic measurement. Journal of Analytical Atomic Spectrometry 30(4), 957-966.

23. Jeremiason, J.D., Kanne, L.A., Lacoe, T.A., Hulting, M. and Simcik, M.F. (2009) A comparison of mercury cycling in Lakes Michigan and Superior. Journal of Great Lakes Research 35(3), 329-336.

24. Jiskra, M., Guedron, S., Tolu, J., Fritz, S.C., Baker, P.A. and Sonke, J.E. (2022) Climatic Controls on a Holocene Mercury Stable Isotope Sediment Record of Lake Titicaca. Acs Earth and Space Chemistry 6(2), 346-357.

25. Jiskra, M., Heimburger-Boavida, L.E., Desgranges, M.M., Petrova, M.V., Dufour, A., Ferreira-Araujo, B., Masbou, J., Chmeleff, J., Thyssen, M., Point, D. and Sonke, J.E. (2021) Mercury stable isotopes constrain atmospheric sources to the ocean. Nature 597(7878), 678-+.

26. Jiskra, M., Wiederhold, J.G., Bourdon, B. and Kretzschmar, R. (2012) Solution Speciation Controls Mercury Isotope Fractionation of Hg(II) Sorption to Goethite. Environmental Science & Technology 46(12), 6654-6662.

27. Jiskra, M., Wiederhold, J.G., Skyllberg, U., Kronberg, R.M., Hajdas, I. and Kretzschmar, R. (2015) Mercury Deposition and Re-emission Pathways in Boreal Forest Soils Investigated with Hg Isotope Signatures. Environmental Science & Technology 49(12), 7188-7196.

28. Jiskra, M., Wiederhold, J.G., Skyllberg, U., Kronberg, R.M. and Kretzschmar, R. (2017) Source tracing of natural organic matter bound mercury in boreal forest runoff with mercury stable isotopes. Environmental Science-Processes & Impacts 19(10), 1235-1248.

29. Jonsson, S., Andersson, A., Nilsson, M.B., Skyllberg, U., Lundberg, E., Schaefer, J.K., Akerblom, S. and Björn, E. (2017) Terrestrial discharges mediate trophic shifts and enhance methylmercury accumulation in estuarine biota. Science Advances 3(1), e1601239.

30. Kurz, A.Y., Blum, J.D., Washburn, S.J. and Baskaran, M. (2019) Changes in the mercury

isotopic composition of sediments from a remote alpine lake in Wyoming, USA. Science of the Total Environment 669, 973-982.

31. Kwon, S.Y., Blum, J.D., Yin, R., Tsui, M.T.K., Yang, Y.H. and Choi, J.W. (2020) Mercury stable isotopes for monitoring the effectiveness of the Minamata Convention on Mercury. Earth-Science Reviews 203, 103111.

32. Lee, J.H., Kwon, S.Y., Yin, R.S., Motta, L.C., Kurz, A.Y. and Nam, S.I. (2021) Spatiotemporal Characterization of Mercury Isotope Baselines and Anthropogenic Influences in Lake Sediment Cores. Global Biogeochemical Cycles 35(10), e2020GB006904.

33. Lepak, R.F., Janssen, S.E., Engstrom, D.R., Krabbenhoft, D.P., Tate, M.T., Yin, R.S., Fitzgerald, W.F., Nagorski, S.A. and Hurley, J.P. (2020) Resolving Atmospheric Mercury Loading and Source Trends from Isotopic Records of Remote North American Lake Sediments. Environmental Science & Technology 54(15), 9325-9333.

34. Lepak, R.F., Yin, R.S., Krabbenhoft, D.P., Ogorek, J.M., DeWild, J.F., Holsen, T.M. and Hurley, J.P. (2015) Use of Stable Isotope Signatures to Determine Mercury Sources in the Great Lakes. Environmental Science & Technology Letters 2(12), 335-341.

35. Li, K., Lin, C.J., Yuan, W., Sun, G.Y., Fu, X.W. and Feng, X.B. (2019) An improved method for recovering and preconcentrating mercury in natural water samples for stable isotope analysis. Journal of Analytical Atomic Spectrometry 34(11), 2303-2313.

36. Lindberg, S., Bullock, R., Ebinghaus, R., Engstrom, D., Feng, X.B., Fitzgerald, W., Pirrone, N., Prestbo, E. and Seigneur, C. (2007) A synthesis of progress and uncertainties in attributing the sources of mercury in deposition. Ambio 36(1), 19-32.

37. Lindqvist, O., Johansson, K., Aastrup, M., Andersson, A., Bringmark, L., Hovsenius, G., Hakanson, L., Iverfeldt, A., Meili, M. and Timm, B. (1991) Mercury in the Swedish Environment - Recent Research on Causes, Consequences and Corrective Methods. Water Air and Soil Pollution 55(1-2), R11-+.

38. Liu, M.D., Zhang, Q.R., Ge, S.D., Mason, R.P., Luo, Y., He, Y.P., Xie, H., Sa, R., Chen, L. and Wang, X.J. (2019) Rapid Increase in the Lateral Transport of Trace Elements Induced by Soil Erosion in Major Karst Regions in China. Environmental Science & Technology 53(8), 4206-4214.

39. Liu, M.D., Zhang, Q.R., Luo, Y., Mason, R.P., Ge, S.D., He, Y.P., Yu, C.H., Sa, R.N., Cao, H.L., Wang, X. and Chen, L. (2018) Impact of Water-Induced Soil Erosion on the Terrestrial Transport and Atmospheric Emission of Mercury in China. Environmental Science & Technology 52(12), 6945-6956.

40. Motta, L.C., Kritee, K., Blum, J.D., Tsui, M.T.K. and Reinfelder, J.R. (2020) Mercury Isotope Fractionation during the Photochemical Reduction of Hg(II) Coordinated with Organic Ligands. Journal of Physical Chemistry A 124(14), 2842-2853.

41. Peterson, C. and Gustin, M. (2008) Mercury in the air, water and biota at the Great Salt Lake (Utah, USA). Science of the Total Environment 405(1-3), 255-268.

42. Powers, S.M., Bruulsema, T.W., Burt, T.P., Chan, N.I., Elser, J.J., Haygarth, P.M., Howden, N.J.K., Jarvie, H.P., Lyu, Y., Peterson, H.M., Sharpley, A.N., Shen, J.B., Worrall, F. and Zhang, F.S. (2016) Long-term accumulation and transport of anthropogenic phosphorus in three river basins. Nature Geoscience 9(5), 353-+.

43. Rolison, J.M., Landing, W.M., Luke, W., Cohen, M. and Salters, V.J.M. (2013) Isotopic composition of species-specific atmospheric Hg in a coastal environment. Chemical Geology 336, 37-49.

44. Schartup, A.T., Balcom, P.H., Soerensen, A.L., Gosnell, K.J., Calder, R.S.D., Mason, R.P. and Sunderland, E.M. (2015) Freshwater discharges drive high levels of methylmercury in Arctic marine biota. Proceedings of the National Academy of Sciences of the United States of America 112(38), 11789-11794.

45. Sherman, L.S., Blum, J.D., Johnson, K.P., Keeler, G.J., Barres, J.A. and Douglas, T.A. (2010) Mass-independent fractionation of mercury isotopes in Arctic snow driven by sunlight. Nature Geoscience 3(3), 173-177.

46. Sun, G.Y., Feng, X.B., Yin, R.S., Wang, F.Y., Lin, C.J., Li, K. and Sommar, J.O. (2022) Dissociation of Mercuric Oxides Drives Anomalous Isotope Fractionation during Net Photo-oxidation of Mercury Vapor in Air. Environmental Science & Technology 56(18), 13428-13438.

47. Sun, R.Y., Enrico, M., Heimburger, L.E., Scott, C. and Sonke, J.E. (2013) A double-stage tube furnace-acid-trapping protocol for the pre-concentration of mercury from solid samples for isotopic analysis. Analytical and Bioanalytical Chemistry 405(21), 6771-6781.

48. Swain, E.B., Engstrom, D.R., Brigham, M.E., Henning, T.A. and Brezonik, P.L. (1992) Increasing Rates of Atmospheric Mercury Deposition in Midcontinental North-America. Science 257(5071), 784-787.

49. Tsui, M.T.K., Blum, J.D. and Kwon, S.Y. (2020) Review of stable mercury isotopes in ecology and biogeochemistry. Science of the Total Environment 716, 135386.

50. Ullrich, S.M., Tanton, T.W. and Abdrashitova, S.A. (2001) Mercury in the aquatic environment: A review of factors affecting methylation. Critical Reviews in Environmental Science and Technology 31(3), 241-293.

51. Vette, A.F., Landis, M.S. and Keeler, G.J. (2002) Deposition and emission of gaseous mercury to and from Lake Michigan during the Lake Michigan Mass Balance Study (July, 1994 October, 1995). Environmental Science & Technology 36(21), 4525-4532.

52. Wang, X., Luo, J., Yin, R.S., Yuan, W., Lin, C.J., Sommar, J., Feng, X.B., Wang, H.M. and Lin, C. (2017) Using Mercury Isotopes To Understand Mercury Accumulation in the Montane Forest Floor of the Eastern Tibetan Plateau. Environmental Science & Technology 51(2), 801-809.

53. Washburn, S.J., Blum, J.D., Motta, L.C., Bergquist, B.A. and Weiss-Penzias, P. (2021) Isotopic Composition of Hg in Fogwaters of Coastal California. Environmental Science & Technology Letters 8(1), 3-8.

54. Wiederhold, J.G., Cramer, C.J., Daniel, K., Infante, I., Bourdon, B. and Kretzschmar, R. (2010) Equilibrium Mercury Isotope Fractionation between Dissolved Hg(II) Species and Thiol-Bound Hg. Environmental Science & Technology 44(11), 4191-4197.

55. Wu, X., Fu, X.W., Zhang, H., Tang, K.H., Wang, X., Zhang, H., Deng, Q.W., Zhang, L.M., Liu, K.Y., Wu, Q.R., Wang, S.X. and Feng, X.B. (2023) Changes in Atmospheric Gaseous Elemental Mercury Concentrations and Isotopic Compositions at Mt. Changbai During 2015-2021 and Mt. Ailao During 2017-2021 in China. Journal of Geophysical Research-Atmospheres 128(10), e2022JD037749.

56. Xia, J.C., Wang, J.X., Zhang, L.M., Wang, X., Yuan, W., Anderson, C.W.N., Chen, C.Y., Peng, T. and Feng, X.B. (2021) Significant mercury efflux from a Karst region in Southwest China - Results from mass balance studies in two catchments. Science of the Total Environment 769, 144892.

57. Zhang, H., Fu, X.W., Wu, X., Deng, Q.W., Tang, K.H., Zhang, L.M., Sommar, J., Sun, G.Y. and Feng, X.B. (2023) Using Mercury Stable Isotopes to Quantify Bidirectional Water-Atmosphere Hg(0) Exchange Fluxes and Explore Controlling Factors. Environmental Science & Technology 57(29), 10673-10685.

58. Zhang, H., Wu, X., Deng, Q.W., Zhang, L.M., Fu, X.W. and Feng, X.B. (2021) Extraction of ultratrace dissolved gaseous mercury and reactive mercury in natural freshwater for stable isotope analysis. Journal of Analytical Atomic Spectrometry 36(9), 1921-1932.

59. Zhang, K., Zheng, W., Sun, R.Y., He, S., Shuai, W.C., Fan, X.F., Yuan, S.L., Fu, P.Q., Deng, J.J., Li, X.D., Wang, S.X. and Chen, J.B. (2022) Stable Isotopes Reveal Photoreduction of Particle-Bound Mercury Driven by Water-Soluble Organic Carbon during Severe Haze. Environmental Science & Technology 56(15), 10619-10628.

60. Zhang, L.M., Wright, L.P. and Blanchard, P. (2009) A review of current knowledge concerning dry deposition of atmospheric mercury. Atmospheric Environment 43(37), 5853-5864.

61. Zheng, W. and Hintelmann, H. (2009) Mercury isotope fractionation during photoreduction in natural water is controlled by its Hg/DOC ratio. Geochimica Et Cosmochimica Acta 73(22), 6704-6715.

62. Zheng, W. and Hintelmann, H. (2010) Isotope Fractionation of Mercury during Its Photochemical Reduction by Low-Molecular-Weight Organic Compounds. Journal of Physical Chemistry A 114(12), 4246-4253.

Figure Captions

Fig. 1. Location of the study area and sampling sites in Hongfeng Lake watershed.

Fig. 2. Hg isotope composition of various environmental media collected in the present study.

Fig. 3. Depth profiles of lake water Hg species concentrations and stable isotope composition in HFL.

Fig. 4. Hg stable isotopic compositions of dissolved Hg (DHg) and particulate Hg (PHg) in different environment media in the HFL.

Fig. 5. A Hg mass balance in the HFL ecosystem as revealed by a mass balance and isotope mass balance model.

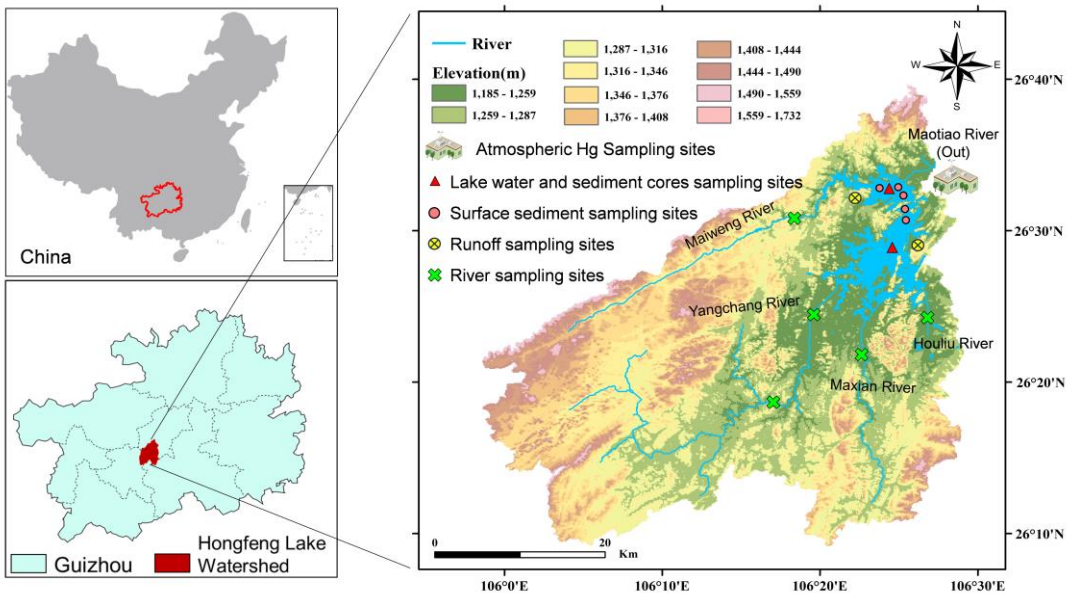

Fig. 1. Location of the study area and sampling sites in Hongfeng Lake watershed.

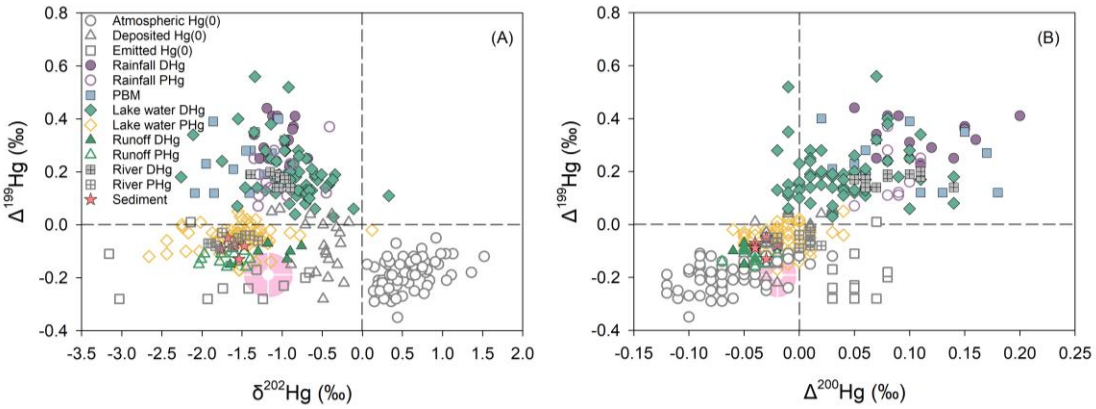

Fig. 2. Hg isotope composition of various environmental media collected in the present study. Panel (A), Odd-isotope independent fractionation ($\Delta^{199}Hg$) versus mass dependent fractionation ($\delta^{202}Hg$). Panel (B), Odd-isotope mass independent fractionation ($\Delta^{199}Hg$) versus even-isotope mass independent fractionation ($\Delta^{200}Hg$). The isotopic compositions of atmospheric Hg(0) (Wu et al. 2023), Hg(0) emitted from water, and Hg(0) deposited to water (Zhang et al. 2023) are from the literature. The light pink shaded area represents the isotopic compositions of lake surface sediments in remote areas with large watershed to lake surface ratios (Guédron et al. 2016, Lee et al. 2021, Lepak et al. 2020).

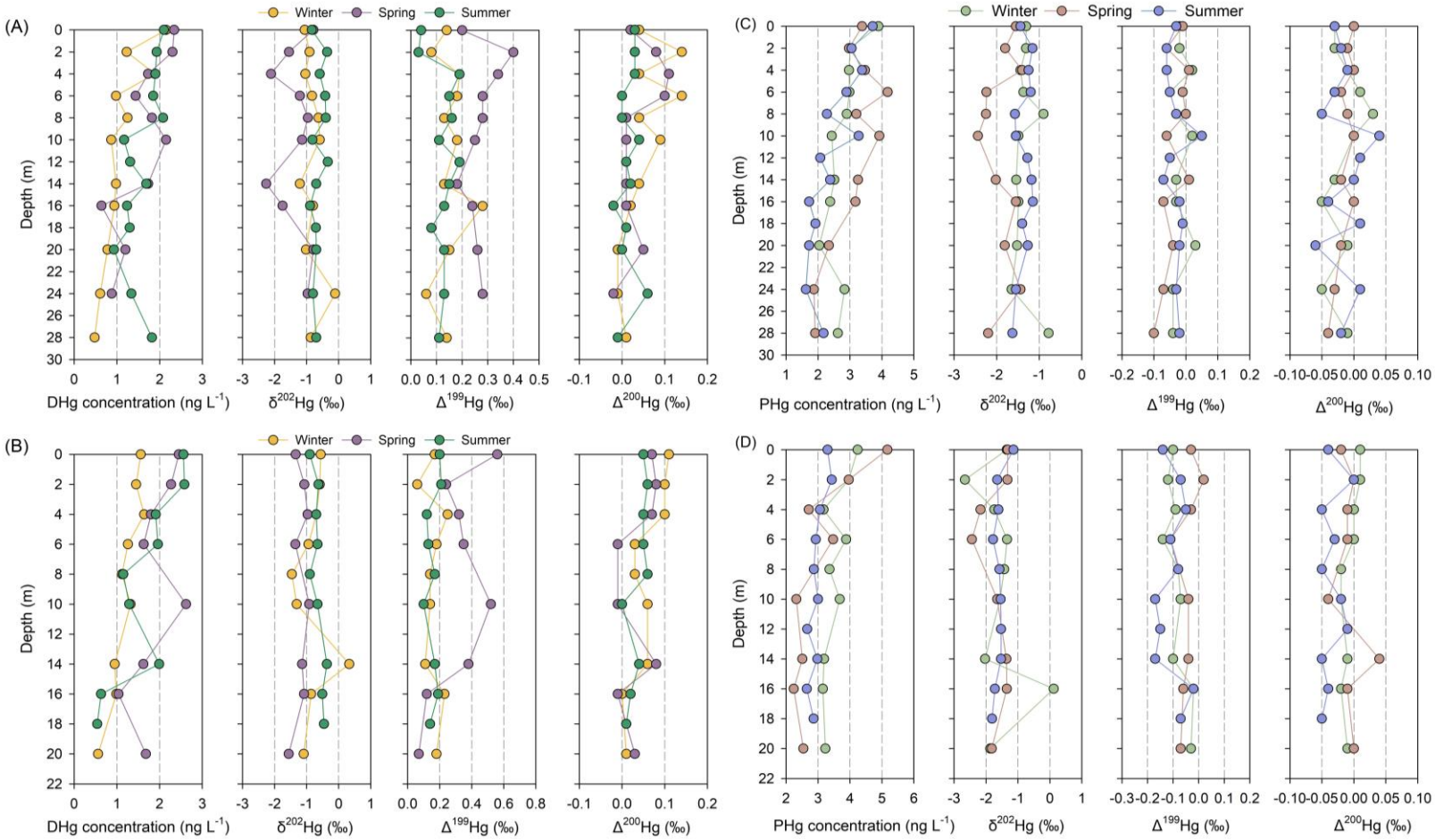

Fig. 3. Depth profiles of lake water Hg species concentrations and stable isotope composition in HFL. Panels (A) and (B) represent the DHg isotopes in northern and southern catchments, respectively. Panels (C) and (D) represent the PHg isotopes in northern and southern catchments, respectively.

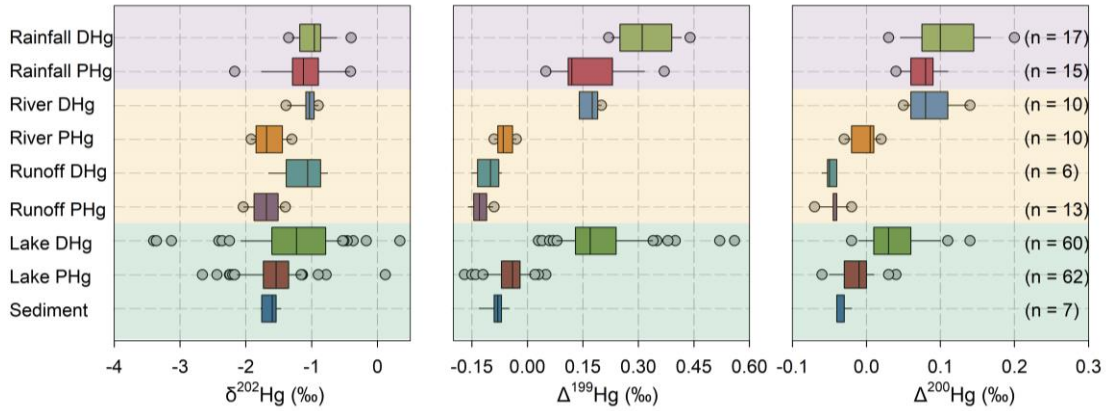

Fig. 4. Hg stable isotopic compositions of dissolved Hg (DHg) and particulate Hg (PHg) in different environment media in the HFL. The light red, light yellow and light green areas represent DHg and PHg for the atmosphere, watershed and lake, respectively. The line in the box indicates the median, the box indicates the IQR, the whiskers indicate the 1.5× the IQR, and outliers are represented by dots.

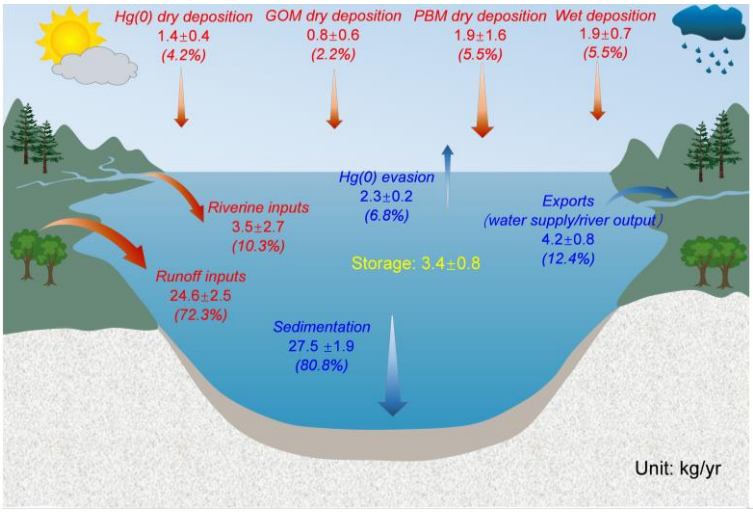

Fig. 5. A Hg mass balance in the HFL ecosystem as revealed by a mass balance and isotope mass balance model. Red and blue colors represent sources and sinks, respectively. Numbers in parentheses represent the relative contribution of each input source.

Supporting Information

Watershed runoff as a dominant pathway for mercury loading into a karst lake as unraveled by a novel mercury isotope and flux balance model

Hui Zhang[a], Xuewu Fu[a,*], Xian Wu[a], Qianwen Deng[a,b], Kaihui Tang[a,b], Leiming Zhang[c], Jonas Olof Sommar[a], Xinbin Feng[a,b]

[a] State Key Laboratory of Environmental Geochemistry, Institute of Geochemistry, Chinese Academy of Sciences, Guiyang, 550081, China

[b] University of Chinese Academy of Sciences, Beijing, 100049, China

[c] Air Quality Research Division, Science and Technology Branch, Environment and Climate Change Canada, Toronto, Ontario, M3H5T4, Canada

**** Corresponding Authors***

E-mail addresses: fuxuewu@mail.gyig.ac.cn (Xuewu Fu)

The supporting information contains:

6 Text Sections

6 Figures

11 Tables

Contents:

Text S1. Water quality parameters, chlorophyll concentration, and dissolved organic carbon at HFL

Three distinct sampling campaigns were conducted in January, March, and July 2020, representing the winter, spring, and summer season, respectively, to capture seasonal variations in HFL Lake. Water samples were collected at 2-meter intervals from various depths across the entire water column to provide a comprehensive representation of the lake's vertical profile. During these campaigns, a range of fundamental physical and chemical properties were measured in situ, including pH, water temperature (T), dissolved oxygen (DO), suspended particulate matter (SPM), chlorophyll-a (Chl-a) substance, and dissolved organic carbon (DOC). These parameters were recorded using a portable multiparameter water quality sonde (YSI EXO2, USA). The concentration of SPM was determined by the cold dry weighing method, while DOC was analyzed using an elemental analyzer (Vario TOC Cube, Germany) (Lee et al. 2019). A detailed summary of the water quality parameters measured in this study is provided in Table S9.

Text S2. Procedures for collecting, processing, and analyzing rainfall samples

The rainfall sampler is equipped with an online standard rain gauge that automatically records the date and the amount of rainfall. Upon the onset of rain, the instrument triggers the opening of a funnel container (PTFE, $\Phi = 300$ mm $\pm$ 0.02 mm) to collect precipitation, and it automatically closes when rainfall ceases, ensuring that only wet deposition samples are collected. Prior to sampling, eight PTFE bottles (1 L capacity) were thoroughly washed through acid leaching and then rinsed three times with ultrapure deionized water to eliminate contaminants. Rainfall samples were filtered immediately after collection through a GF/F filter (Whatman, 2.2 μm pore size) once sufficient precipitation had been collected or after one or two separate precipitation events. The filtered samples were preserved in the field by adding 5‰ (v/v) of race-metal reagent grade HCl and were subsequently stored in PTFE containers at 4°C before undergoing Hg concentration and isotope analysis. To ensure sample integrity, the rainfall samples were generally stored in the sampling bottles for a maximum of three days.

Text S3. Sediment age and rate

A sediment sample, weighing between 5 and 10 grams, was placed in a plastic sample box (Φ 37 mm × 29 mm), sealed with wax, and stored for approximately one month to allow ^{226}Ra and ^{210}Pb to reach decay equilibrium. After this incubation period, the ^{210}Pb activity was measured using a multichannel spectrometer (GX6020, Canberra, USA, with a resolution of less than 2.0 keV) over a measurement time of 16 to 24 hours. The excess ^{210}Pb activity ($^{210}Pb_{ex}$) was obtained by subtracting the ^{226}Ra activity from the measured ^{210}Pb activity. The chronology and sediment accumulation rates were subsequently assessed using the constant flux and sediment rate (CFCS) model (Table S12). This model assumes that the sedimentation flux of ^{210}Pb (F, Bq cm^{-2} a^{-1}) and the sedimentation rate (S, g cm^{-2} a^{-1}) are stable over time. In this framework, the sedimentation rate and the initial specific activity of ^{210}Pb in each sediment layer are treated as constants (F/S). The specific activity of ^{210}Pb is assumed to decay exponentially with time, allowing the specific activity (C, Bq kg^{-1}) of $^{210}Pb_{ex}$ in different sediment layers to be modeled as a function of the sediment mass depth (M, g cm^{-2}), as calculated in the following formula:

$$C = \frac{F}{S} exp^{-(\alpha \times M)} \qquad (1)$$

$$\alpha = \frac{\lambda}{S} \qquad (2)$$

where λ is the decay constant of ^{210}Pb (0.03114 a^{-1}). The dry weight of each sediment layer was calculated by multiplying dry weight density by volume. Considering the compaction of the sediment, the mass depth (g cm^{-2}) was therefore used to calculate the sediment accumulation rate. The mass depth at depth x (M(x)) was calculated using the formula:

$$M(x) = \int_0^x \rho(s) ds \qquad (3)$$

where ρ(s) is the dry bulk density at depth s.

Text S4. Quality assurance and quality control

Blanks and pre-concentration methods were thoroughly evaluated in accordance with standard quality assurance and control protocols. The system blank, which was determined by thermally treating 1g of CLC with 5 mL of a 40% acid solution, yielded a value of 0.05 ± 0.03 ng mL^{-1}, representing less than 3% of the amount loaded from field sampling. The efficiency of CLC in capturing Hg(0) vapor was determined to be 94.5 ± 4.2% (mean ± 1SD, n = 14), a crucial factor in excluding isotopic fractionation (Fu et al. 2014). Recoveries for the pre-concentrated water samples ranged from 90.1 to 110.3%, indicating reliable extraction efficiency. During the Hg isotope measurements, standard reference materials (SRM 3177, RM 8610, BCR 482, and SRM 1947) were analyzed regularly to assess the instrumental uncertainties and the performance of laboratory pre-concentration procedures. This quality control procedure also ensured the accuracy of measurements for each natural environmental sample. The Hg isotope compositions of the standards were found to be in agreement with the reported values (Table S2), further confirming the reliability of the analytical methods.

Text S5. Hg isotope mass balance model

The Hg isotope mass balance model was employed to quantify the sources of Hg input into the lake ecosystem. Hg in lake environments can be derived from multiple sources, including the direct dry deposition of atmospheric gaseous elemental mercury (Hg(0) or GEM), particulate-bound mercury (PBM), and gaseous oxidized mercury (Hg(II) or GOM) to the water, wet deposition of Hg(II), as well as inputs from rivers and surface runoff (Engstrom 2007). Among these, the dry deposition of Hg(0) and wet deposition of Hg(II) were quantified. The atmospheric Hg(0) dry deposition and emission fluxes at HFL were previously quantified using the Δ^{200}Hg mixing model (Zhang et al. 2023), while the atmospheric Hg(II) wet deposition fluxes were derived by multiplying the measured rainfall Hg concentrations (volume-weighted mean precipitation Hg concentration) by the corresponding precipitation volume (Fu et al. 2016). However, the atmospheric Hg(II) and PBM dry deposition, as well as the contributions from riverine and runoff Hg, remain difficult to quantify, and thus, these sources were treated as unknowns in the Hg isotope mass balance model.

For sedimentation flux calculations, sediment cores were collected, and ^{210}Pb was measured in the sediments through multi-channel spectrometry to determine the sediment age. The sedimentation rate was then calculated using the constant flux and sediment rate (CFCS) model, and the sedimentation flux of Hg was calculated from the surface sediment Hg concentrations. The water Hg(0) evasion flux and isotopic compositions were obtained from Zhang et al. (Zhang et al. 2023). The Hg export flux from HFL, via the Maotiao River and water supply, was estimated based on Hg concentrations and water mass flux data, which were sourced from the Guiyang City Water Resources Bulletin (2020).

The isotopic compositions for precipitation Hg, PBM, riverine Hg, and runoff Hg were measured in the present study. The isotopic data of atmospheric Hg(0) were adopted from Wu et al. (Wu et al. 2023) based on observations for Chinese forests and those of gaseous Hg(II) were obtained from Araujo et al. (Araujo et al. 2022) based on Hg(II) data collected using a polyethersulfone (PES) cation-exchange membrane method, nothing that field GOM data were very limited due to the difficulty in collecting gaseous Hg(II)(). Using the Hg isotope mass balance model, the mass fluxes of Hg input from PBM, gaseous Hg(II), and river and surface runoff to the lake were calculated. Furthermore, the relative contributions of each Hg source to the overall Hg input to the lake were determined.

Monte Carlo simulations generated one million sets of signals with a random range of different input sources (atmospheric dry and wet deposition, watershed rivers, and runoff), of which the median and IQR were considered, to analyze the uncertainty caused by the deviations in signals from the different input sources on the computed proportions.

Text S6. The endmember mixing model

To quantify the sources of Hg in sediments, binary mixing models were utilized. The primary source of Hg in sediments is the deposition of particulate matter from the water column. Additionally, surface sediments may adsorb dissolved Hg (DHg). Previous studies have confirmed that Hg sedimentation and adsorption processes do not affect odd- and even-MIF Hg signatures (Jiskra et al. 2012, Wiederhold et al. 2010). The decision to exclude Δ^{200}Hg isotopic signatures in this study was justified by the small differences between DHg and particulate Hg (PHg) in the water column, which hinder effective differentiation of their respective contributions to sedimentary Hg. Consequently, the Δ^{199}Hg mixing model was applied to assess the relative proportions of DHg and PHg contributing to Hg accumulation in lake sediments.

$$f_{DHg} + f_{PHg} = 1 \quad (4)$$

$$f_{DHg} \times \Delta^{199}Hg_{DHg} + f_{PHg} \times \Delta^{199}Hg_{PHg} = \Delta^{199}Hg_{Sediment} \quad (5)$$

where f_{DHg} and f_{PHg} represent the proportions of lake DHg and PHg in sediment respectively.

Monte Carlo simulations generated one million sets of even-MIF signatures with random ranges, of which median and IQR were taken into account to analyze the uncertainty in the calculated proportions caused by deviations in the odd-MIF signatures.

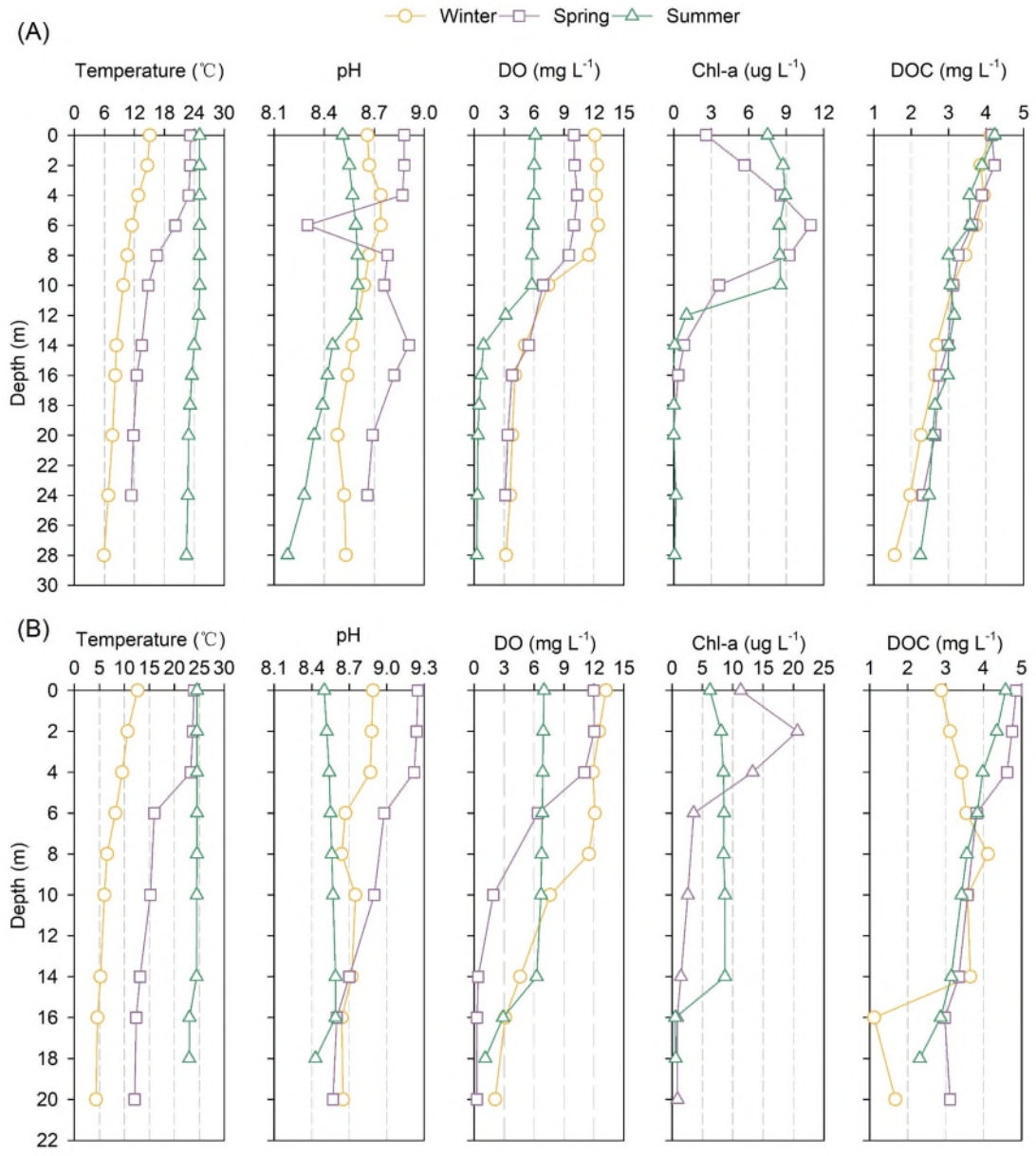

Figure S1. Physicochemical parameters of water samples collected from Hongfeng lake: (A) the northern basin, and (B) the southern basin.

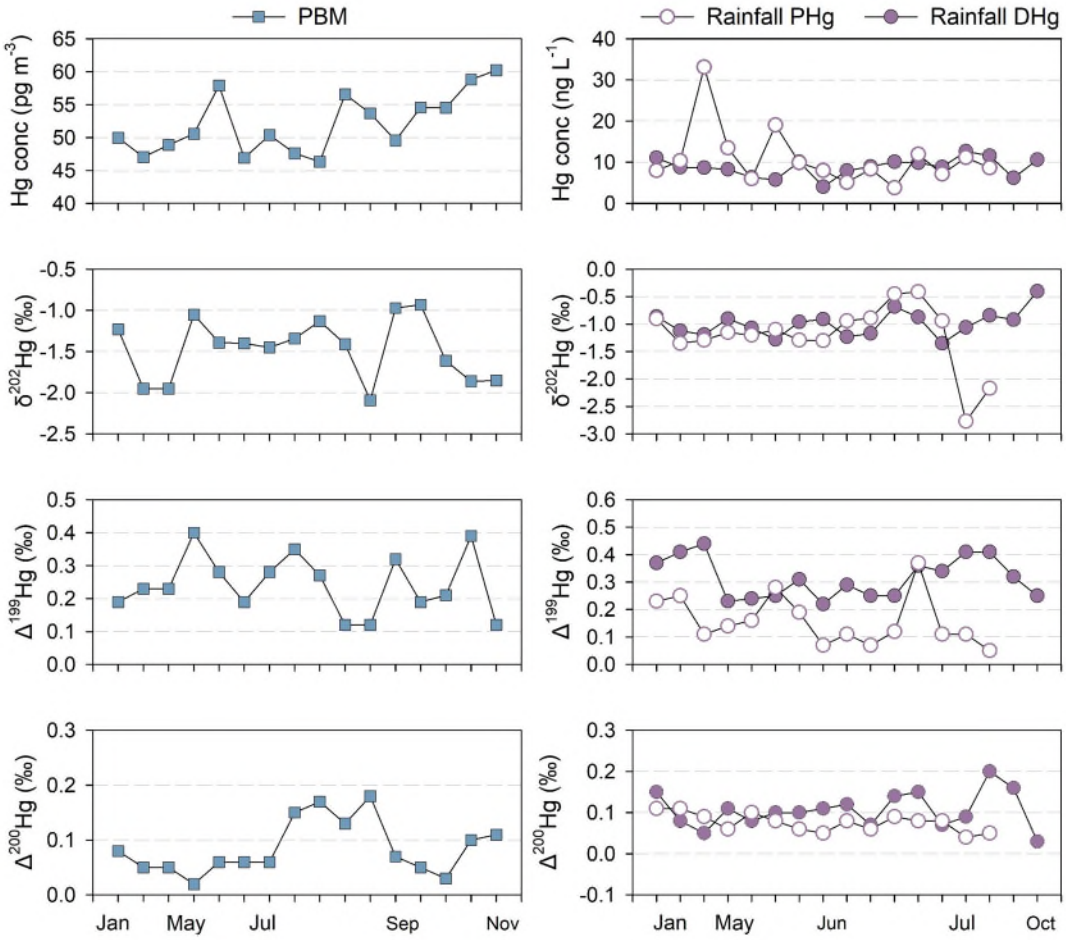

Figure S2. Seasonal variability in PBM and precipitation Hg(II) concentrations and isotopic composition of HFL.

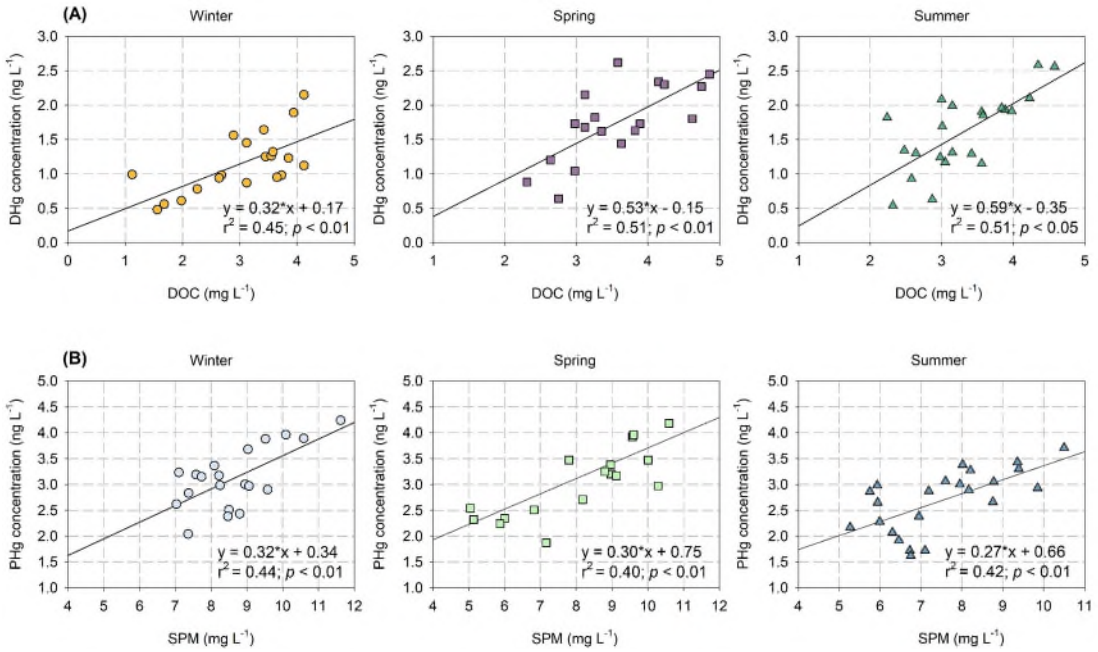

Figure S3. The linear relationship between DHg concentration and DOC concentration (A) and between PHg concentration and SPM concentration (B) throughout the water column during three (Winter, Spring, Summer) sampling campaigns.

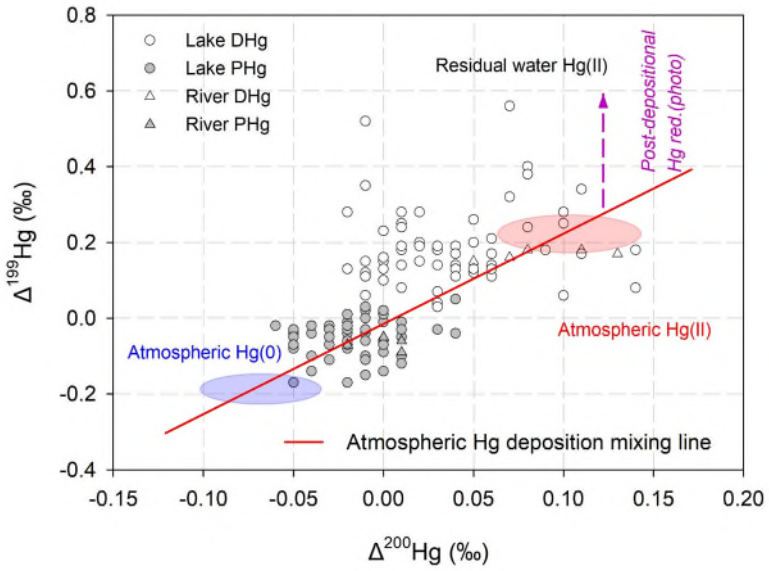

Figure S4. Odd-isotope mass independent fractionation (Δ^{199}Hg) versus even-isotope mass independent fractionation (Δ^{200}Hg) of river and lake water. Atmospheric Hg(0) data (blue shading, median and IQR) are from the literature (Wu et al. 2023), and atmospheric Hg(II) data (red shading, median and IQR) are resulted from the mixing of precipitation Hg(II) and PBM in this study. The upward solid purple arrow represents the trajectories of residual Hg(II) in the water column after Hg(0) emission mediated by the photochemical reduction process (Zhang et al. 2023).

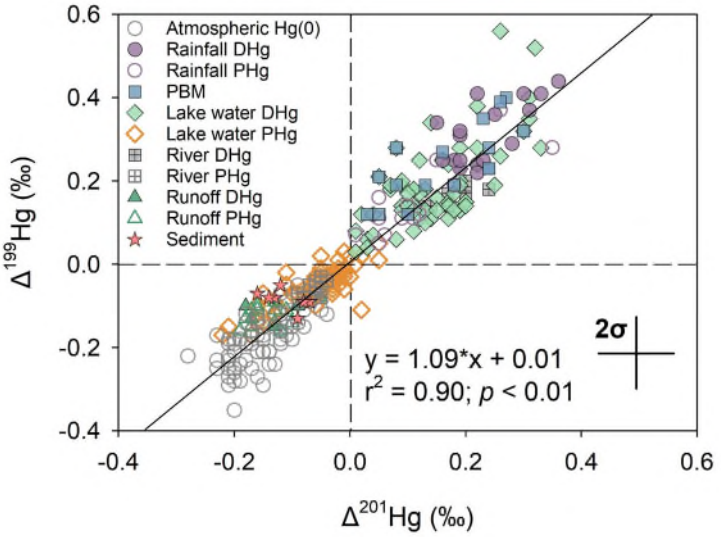

189

190 **Figure S5.** Linear correlations between Δ^{201}Hg and Δ^{199}Hg in atmospheric Hg(0) (Wu et al. 2023),
191 Hg(II), river water, lake water, runoff, and sediment samples in HFL ecosystem.

192

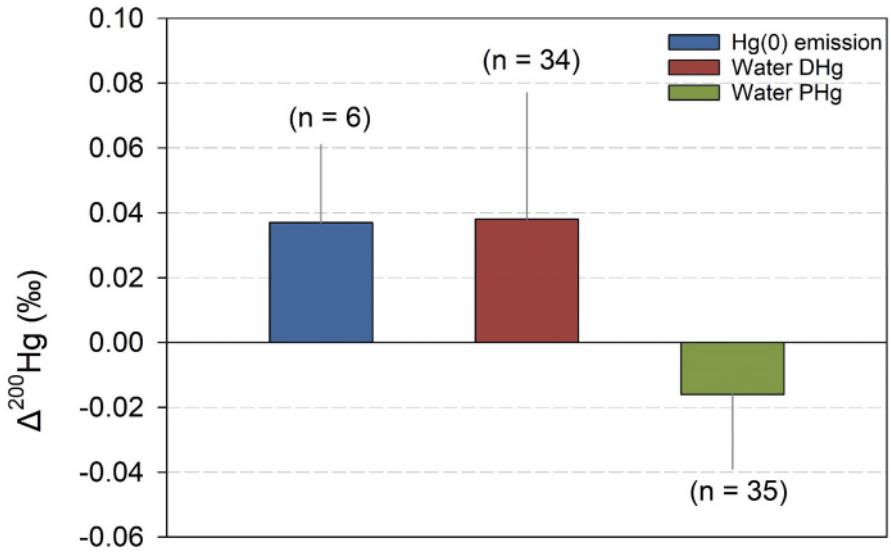

Figure S6. Comparison of Δ^{200}Hg isotopic signatures of DHg, PHg, and Hg(0) emission in lake water of HFL.

Table S1. Mass balance components in HFL.

Geographical data	**Surface area: 57.2 km^2, Watershed area: 1596km^2, Max depth: 45m, Altitude: 1230m, Water transparency: 2m**	
Media	**(kg Hg/year)**	**Description**
Inputs (Sources)		
Wet deposition	1.87±0.67	The flux of Hg wet deposition was calculated by multiplying the volume-weighted average Hg concentration in precipitation by the cumulative annual precipitation depth (Fu et al. 2016)
Hg(0) dry deposition	1.43±0.37	The fluxes of Hg(0) dry deposition and Hg(0) evasion from water, along with their respective isotopic compositions, were derived from the methodology outlined by Zhang et al. (Zhang et al. 2023)
GOM dry deposition		Because of the large uncertainties in the influxes and dry Hg(II) deposition velocities, these four sources were used in a Hg isotope mass balance model to estimate the proportion of Hg inputs to the lake ecosystem.
PBM dry deposition		
Riverine input		
Runoff input		
Total		
Outputs (Sinks)		
Sediment loss	27.54±1.85	The sedimentation flux of Hg was determined by considering the Hg concentration in surface sediments and the sedimentation rate over the past decade (~ 10 years). The sediment accumulation rate was determined by ^{210}Pb and ^{137}Cs analysis (Table S11)
Volatile loss	2.30±0.15	The fluxes of Hg(0) dry deposition and Hg(0) evasion from water, along with their respective isotopic compositions, were derived from the methodology outlined by Zhang et al. (Zhang et al. 2023)
Water supply	0.63±0.15	Hg export through the downstream river and municipal water supply was estimated based on the concentrations of Hg in the water and corresponding water flow rates. Water flow data from Guiyang City Water Resources Bulletin 2020
Export to river	3.60±0.84	
Total	**34.08**	

Table S2. Statistical results of the average isotopic compositions of Hg standard for NIST SRM 3177, RM 8610, BCR 482, and SRM 1947 over Hg isotope analytical sessions in this study.

Hg standard	Material	n	Recovery	1SD	$\delta^{199}Hg$	2SD	$\delta^{200}Hg$	2SD	$\delta^{201}Hg$	2SD	$\delta^{202}Hg$	2SD	$\delta^{204}Hg$	2SD	$\Delta^{199}Hg$	2SD	$\Delta^{200}Hg$	2SD	$\Delta^{201}Hg$	2SD	$\Delta^{204}Hg$	2SD
			%		(‰)		(‰)		(‰)		(‰)		(‰)		(‰)		(‰)		(‰)		(‰)	
NIST SRM 3177[a]	Standard solution	18			-0.13	0.06	-0.26	0.05	-0.39	0.08	-0.51	0.07	-0.74	0.14	-0.01	0.06	0.00	0.05	-0.00	0.06	0.01	0.11
RM 8610[a]	Standard solution	45			-0.15	0.07	-0.25	0.06	-0.41	0.09	-0.52	0.07	-0.77	0.13	-0.01	0.06	0.01	0.05	-0.02	0.07	0.01	0.12
BCR 482[b]	Lichen	29	97.23	6.48	-1.05	0.11	-0.73	0.09	-1.84	0.11	-1.60	0.12	-2.44	0.24	-0.64	0.10	0.07	0.04	-0.64	0.12	-0.05	0.15
SRM 1947[b]	Fish	9	97.00	4.97	5.52	0.11	0.64	0.11	4.94	0.16	1.13	0.14	1.57	0.20	5.23	0.08	0.07	0.05	4.09	0.12	-0.13	0.19

a): The isotopic compositions of standard references NIST SRM and RM 8610 were measured simultaneously to reflect the analytical uncertainty of instrumental procedures during Hg isotope analysis session.

b): Combustion of BCR 482 and SRM 1947 using the two-stage furnace system. The isotopic compositions of standard references BCR 482 and SRM 1947 were measured repeatedly to reflect the analytical uncertainty of instrumental procedures and thermal processing.

The analytical uncertainty (2SD, two times of standard error) for Hg isotopic compositions in this study is reported as the larger value of either 2SD of the reproducibility of the procedural RM 8610 or 2SD of the repeated analysis of the sample.

Table S3. Hg concentration and isotope compositions of atmospheric precipitation samples (dissolved (DHg) and particulate (PHg) Hg) in HFL.

Sample ID	Sampling time	Hg conc	δ^{202}Hg	Δ^{199}Hg	Δ^{200}Hg	Δ^{201}Hg	Δ^{204}Hg	δ^{202}Hg	Δ^{199}Hg	Δ^{200}Hg	Δ^{201}Hg	Δ^{204}Hg
		ng L^{-1}	‰	‰	‰	‰	‰	2SD	2SD	2SD	2SD	2SD
R-DHg	2020/3	11.06	-0.86	0.37	0.15	0.31	-0.17	0.07	0.06	0.05	0.07	0.12
R-DHg-1	2020/4	8.77	-1.12	0.41	0.08	0.33	-0.16	0.07	0.06	0.05	0.07	0.12
R-DHg-2	2020/4	8.67	-1.19	0.44	0.05	0.36	-0.13	0.07	0.06	0.05	0.07	0.12
R-DHg	2020/5	8.27	-0.90	0.23	0.11	0.19	-0.11	0.10	0.06	0.06	0.08	0.12
R-DHg-1	2020/6	6.33	-1.07	0.24	0.08	0.22	0.10	0.07	0.06	0.05	0.07	0.12
R-DHg-2	2020/6	5.76	-1.28	0.25	0.10	0.23	-0.24	0.07	0.06	0.05	0.07	0.12
R-DHg-3	2020/6	10.15	-0.96	0.31	0.10	0.19	-0.24	0.07	0.06	0.05	0.07	0.12
R-DHg-4	2020/6	4.03	-0.91	0.22	0.11	0.22	-0.21	0.07	0.06	0.05	0.07	0.12
R-DHg-5	2020/6	7.93	-1.23	0.29	0.12	0.28	-0.09	0.07	0.06	0.05	0.07	0.12
R-DHg-6	2020/6	8.97	-1.17	0.25	0.07	0.18	-0.19	0.07	0.06	0.05	0.07	0.12
R-DHg-1	2020/7	10.12	-0.68	0.25	0.14	0.16	-0.23	0.07	0.06	0.05	0.07	0.12
R-DHg-2	2020/7	9.87	-0.87	0.36	0.15	0.25	0.03	0.07	0.06	0.05	0.07	0.12
R-DHg-3	2020/7	8.85	-1.35	0.34	0.07	0.15	-0.11	0.07	0.06	0.05	0.07	0.12
R-DHg-1	2020/8	12.65	-1.06	0.41	0.09	0.30	-0.10	0.09	0.06	0.05	0.07	0.15
R-DHg-2	2020/8	11.58	-0.84	0.41	0.20	0.22	-0.11	0.07	0.07	0.07	0.07	0.12
R-DHg-3	2020/8	6.21	-0.92	0.32	0.16	0.19	-0.10	0.07	0.07	0.07	0.07	0.12
R-DHg	2020/10	10.64	-0.40	0.25	0.03	0.19	-0.05	0.08	0.06	0.05	0.07	0.30
R-PHg	2020/3	7.97	-0.90	0.23	0.11	0.19	-0.11	0.10	0.06	0.06	0.08	0.12
R-PHg	2020/4	10.36	-1.35	0.25	0.11	0.15	-0.21	0.07	0.06	0.05	0.07	0.12
R-PHg	2020/5	33.09	-1.29	0.11	0.09	0.09	-0.17	0.07	0.06	0.05	0.07	0.12
R-PHg-1	2020/6	13.47	-1.15	0.14	0.06	0.10	-0.15	0.07	0.06	0.05	0.07	0.12
R-PHg-2	2020/6	5.98	-1.20	0.16	0.10	0.05	-0.12	0.07	0.06	0.05	0.07	0.12
R-PHg-3	2020/6	19.05	-1.10	0.28	0.08	0.35	-0.17	0.08	0.06	0.05	0.07	0.12
R-PHg-4	2020/6	9.91	-1.29	0.19	0.06	0.18	-0.12	0.08	0.06	0.05	0.07	0.12
R-PHg-5	2020/6	7.97	-1.30	0.07	0.05	0.01	-0.13	0.08	0.06	0.05	0.07	0.12
R-PHg-6	2020/6	5.09	-0.94	0.11	0.08	0.11	-0.26	0.07	0.06	0.05	0.07	0.12
R-PHg-7	2020/6	8.34	-0.89	0.07	0.06	0.06	-0.09	0.07	0.06	0.05	0.07	0.12
R-PHg-8	2020/6	3.79	-0.45	0.12	0.09	0.12	-0.11	0.15	0.09	0.05	0.07	0.12
R-PHg-9	2020/6	11.92	-0.41	0.37	0.08	0.26	-0.43	0.07	0.06	0.05	0.07	0.12
R-PHg	2020/7	7.12	-0.94	0.11	0.08	0.11	-0.26	0.07	0.06	0.05	0.07	0.12
R-PHg	2020/8	11.15	-2.77	0.11	0.04	0.05	-0.11	0.07	0.10	0.06	0.07	0.12
R-PHg	2020/10	8.65	-2.17	0.05	0.05	0.05	-0.06	0.07	0.10	0.06	0.07	0.12

Table S4. Hg concentration and isotope compositions of atmospheric PBM samples in HFL.

Sample ID	Start time	End time	PBM	$\delta^{202}Hg$	$\Delta^{199}Hg$	$\Delta^{200}Hg$	$\Delta^{201}Hg$	$\Delta^{204}Hg$	$\delta^{202}Hg$	$\Delta^{199}Hg$	$\Delta^{200}Hg$	$\Delta^{201}Hg$	$\Delta^{204}Hg$
			pg m^{-3}	‰	‰	‰	‰	‰	2SD	2SD	2SD	2SD	2SD
PBM-1	2019/12/30	2020/12/31	46.82	--	--	--	--	--	--	--	--	--	--
PBM-2	2020/1/17	2020/1/19	49.96	-1.23	0.19	0.08	0.08	0.00	0.07	0.06	0.05	0.07	0.12
PBM-3	2020/4/5	2020/4/7	48.43	--	--	--	--	--	--	--	--	--	--
PBM-4	2020/4/15	2020/4/17	47.06	-1.95	0.23	0.05	0.24	-0.05	0.07	0.06	0.05	0.07	0.12
PBM-5	2020/4/23	2020/4/25	48.89	-1.95	0.23	0.05	0.24	-0.05	0.07	0.06	0.05	0.07	0.12
PBM-6	2020/5/9	2020/5/11	50.57	-1.05	0.40	0.02	0.27	-0.14	0.07	0.06	0.05	0.07	0.12
PBM-7	2020/5/11	2020/5/13	57.90	-1.39	0.28	0.06	0.08	-0.30	0.08	0.06	0.05	0.07	0.12
PBM-8	2020/5/22	2020/5/24	46.90	-1.40	0.19	0.06	0.13	-0.10	0.07	0.06	0.05	0.07	0.12
PBM-9	2020/6/10	2020/6/12	50.37	-1.45	0.28	0.06	0.24	-0.27	0.07	0.06	0.05	0.07	0.12
PBM-10	2020/6/16	2020/6/18	47.61	-1.34	0.35	0.15	0.23	-0.20	0.08	0.06	0.05	0.07	0.12
PBM-11	2020/7/4	2020/7/6	46.33	-1.13	0.27	0.17	0.16	-0.30	0.07	0.06	0.05	0.07	0.12
PBM-12	2020/7/28	2020/7/30	50.95	--	--	--	--	--	--	--	--	--	--
PBM-13	2020/8/12	2020/8/14	56.57	-1.41	0.12	0.13	0.10	-0.17	0.07	0.06	0.06	0.07	0.12
PBM-14	2020/8/27	2020/8/29	53.69	-2.09	0.12	0.18	0.03	-0.16	0.07	0.06	0.05	0.07	0.12
PBM-15	2020/9/8	2020/9/10	49.56	-0.97	0.32	0.07	0.30	0.03	0.07	0.06	0.06	0.17	0.12
PBM-16	2020/9/18	2020/9/20	54.56	-0.93	0.19	0.05	0.18	-0.07	0.10	0.07	0.06	0.07	0.12
PBM-17	2020/10/8	2020/10/10	54.53	-1.61	0.21	0.03	0.05	-0.11	0.07	0.06	0.05	0.07	0.12
PBM-18	2020/10/19	2020/10/21	58.82	-1.86	0.39	0.10	0.26	-0.08	0.07	0.06	0.05	0.07	0.12
PBM-19	2020/10/28	2020/10/30	60.24	-1.85	0.12	0.11	0.05	-0.16	0.07	0.06	0.05	0.07	0.12

Table S5. Hg concentration and isotope compositions of water samples from four rivers, including the Maiweng river (MW), Yangchang river (YC), Maxian river (MX), and Houliu river (HL), that enter the HFL.

Sample ID	Sampling time	Hg conc	$\delta^{202}Hg$	$\Delta^{199}Hg$	$\Delta^{200}Hg$	$\Delta^{201}Hg$	$\Delta^{204}Hg$	$\delta^{202}Hg$	$\Delta^{199}Hg$	$\Delta^{200}Hg$	$\Delta^{201}Hg$	$\Delta^{204}Hg$
		ng L^{-1}	‰	‰	‰	‰	‰	2SD	2SD	2SD	2SD	2SD
MW-DHg-1	2021/3	3.05	-0.98	0.18	0.11	0.20	-0.15	0.08	0.06	0.06	0.07	0.12
MW-DHg-2	2021/7	3.58	-1.07	0.19	0.10	0.20	-0.06	0.08	0.06	0.06	0.07	0.12
YC-DHg-1-1	2021/3	3.76	-1.07	0.14	0.07	0.12	-0.04	0.07	0.06	0.09	0.10	0.12
YC-DHg-2-1	2021/7	3.58	-0.95	0.17	0.06	0.20	0.11	0.08	0.06	0.07	0.07	0.12
YC-DHg-1-2	2021/3	5.97	-1.03	0.18	0.08	0.24	-0.23	0.08	0.08	0.05	0.07	0.27
YC-DHg-2-2	2021/7	6.02	-1.39	0.19	0.08	0.20	-0.36	0.08	0.08	0.05	0.07	0.27
MX-DHg-1	2021/3	3.05	-0.97	0.17	0.05	0.17	-0.17	0.12	0.06	0.06	0.07	0.12
MX-DHg-2	2021/7	2.98	-0.90	0.14	0.06	0.17	0.19	0.12	0.06	0.06	0.07	0.12
HL-DHg-1	2021/3	4.20	-1.04	0.14	0.14	0.14	-0.37	0.08	0.06	0.06	0.07	0.12
HL-DHg-2	2021/7	4.08	-1.15	0.20	0.11	0.20	-0.20	0.07	0.07	0.06	0.07	0.21
MW-PHg-1	2021/3	8.27	-1.75	-0.03	0.01	-0.05	-0.01	0.07	0.07	0.06	0.07	0.21
MW-PHg-2	2021/7	8.42	-1.83	-0.08	0.01	-0.08	0.04	0.07	0.07	0.06	0.07	0.21
YC-PHg-1-1	2021/3	6.89	-1.55	-0.05	-0.02	-0.11	0.10	0.08	0.06	0.07	0.07	0.12
YC-PHg-2-1	2021/7	6.67	-1.46	-0.04	0.01	-0.09	-0.20	0.08	0.06	0.07	0.07	0.12
YC-PHg-1-2	2021/3	9.96	-1.92	-0.07	-0.03	-0.09	0.00	0.08	0.08	0.05	0.07	0.27
YC-PHg-2-2	2021/7	9.98	-1.89	-0.07	-0.02	-0.06	-0.03	0.07	0.06	0.09	0.10	0.12
MX-PHg-1	2021/3	13.69	-1.40	-0.04	0.00	-0.06	0.07	0.12	0.06	0.06	0.07	0.12
MX-PHg-2	2021/7	13.51	-1.30	-0.06	0.01	-0.05	-0.04	0.12	0.06	0.06	0.07	0.12
HL-PHg-1	2021/3	6.80	-1.77	-0.09	0.00	-0.07	-0.14	0.12	0.06	0.06	0.07	0.12
HL-PHg-2	2021/7	6.59	-1.62	-0.08	0.02	-0.05	0.12	0.12	0.06	0.06	0.07	0.12

Table S6. Hg concentration and isotope compositions of runoff samples in HFL.

Sample ID	Sampling time	Hg conc	δ^{202}Hg	Δ^{199}Hg	Δ^{200}Hg	Δ^{201}Hg	Δ^{204}Hg	δ^{202}Hg	Δ^{199}Hg	Δ^{200}Hg	Δ^{201}Hg	Δ^{204}Hg
		ng L^{-1}	‰	‰	‰	‰	‰	2SD	2SD	2SD	2SD	2SD
Runoff-DHg-1	2020/7	19.24	-1.18	-0.07	-0.05	-0.07	0.07	0.07	0.06	0.05	0.07	0.12
Runoff-DHg-2	2020/7	10.94	-1.65	-0.15	-0.06	-0.15	-0.32	0.07	0.06	0.05	0.07	0.12
Runoff-DHg-1	2020/5	16.85	-0.94	-0.13	-0.04	-0.17	0.15	0.07	0.07	0.05	0.07	0.12
Runoff-DHg-2	2020/5	14.65	-0.90	-0.10	-0.06	-0.18	0.05	0.07	0.07	0.05	0.08	0.12
Runoff-DHg-3	2020/5	15.17	-1.30	-0.10	-0.05	-0.09	0.19	0.07	0.07	0.05	0.08	0.12
Runoff-DHg	2020/6	12.14	-0.76	-0.08	-0.04	-0.05	0.12	0.07	0.07	0.05	0.08	0.12
Runoff-PHg-1	2020/7	79.25	-1.40	-0.13	-0.04	-0.18	-0.03	0.07	0.10	0.06	0.07	0.12
Runoff-PHg-2	2020/7	75.75	-1.45	-0.16	-0.04	-0.19	0.01	0.09	0.09	0.05	0.07	0.19
Runoff-PHg-3	2020/7	70.25	-1.73	-0.11	-0.02	-0.13	-0.08	0.08	0.11	0.05	0.10	0.45
Runoff-PHg-4	2020/7	69.56	-2.04	-0.15	-0.03	-0.17	-0.09	0.10	0.06	0.05	0.10	0.12
Runoff-PHg-5	2020/7	65.31	-1.97	-0.11	-0.04	-0.11	-0.02	0.10	0.06	0.05	0.10	0.12
Runoff-PHg-6	2020/7	74.65	-2.01	-0.13	-0.04	-0.17	0.08	0.10	0.06	0.05	0.10	0.12
Runoff-PHg-1	2020/5	77.34	-1.55	-0.14	-0.04	-0.10	0.11	0.07	0.06	0.05	0.07	0.12
Runoff-PHg-2	2020/5	70.45	-1.62	-0.09	-0.05	-0.13	0.17	0.07	0.06	0.05	0.07	0.12
Runoff-PHg-3	2020/5	76.24	-1.69	-0.16	-0.04	-0.12	0.16	0.07	0.06	0.05	0.07	0.12
Runoff-PHg-4	2020/5	79.78	-1.47	-0.10	-0.05	-0.16	-0.03	0.07	0.06	0.05	0.07	0.12
Runoff-PHg-5	2020/5	69.45	-1.60	-0.11	-0.04	-0.17	0.14	0.07	0.06	0.05	0.07	0.12
Runoff-PHg-1	2020/6	69.45	-1.76	-0.11	-0.04	-0.16	-0.03	0.07	0.07	0.05	0.07	0.12
Runoff-PHg-2	2020/6	78.75	-1.78	-0.14	-0.07	-0.13	0.00	0.07	0.07	0.05	0.07	0.12

Table S7. Hg concentration and isotope compositions of litterfall degradation samples in HFL.

Sample ID	Hg conc	$\delta^{202}Hg$	$\Delta^{199}Hg$	$\Delta^{200}Hg$	$\Delta^{201}Hg$	$\Delta^{204}Hg$	$\delta^{202}Hg$	$\Delta^{199}Hg$	$\Delta^{200}Hg$	$\Delta^{201}Hg$	$\Delta^{204}Hg$
	ng L^{-1}	‰	‰	‰	‰	‰	2SD	2SD	2SD	2SD	2SD
Litterfall-1	105.02	-1.71	-0.29	-0.04	-0.23	0.10	0.07	0.06	0.07	0.07	0.12
Litterfall-2	94.80	-1.63	-0.34	-0.04	-0.26	0.14	0.10	0.07	0.07	0.08	0.12
Litterfall-3	90.61	-1.19	-0.38	-0.01	-0.39	-0.15	0.07	0.06	0.07	0.07	0.12
Litterfall-4	120.57	-2.53	-0.09	-0.04	-0.09	-0.09	0.07	0.06	0.08	0.07	0.46
Litterfall-5	110.23	-2.38	-0.06	-0.04	-0.09	0.06	0.07	0.06	0.08	0.07	0.46

Table S8. Concentrations and isotope compositions of dissolved Hg (DHg) in vertical profile in HFL. HFL-N and HFL-S represent the sampling site of northern and southern catchment area, respectively, of Hongfeng lake.

Time	Sample ID	Depth	Tem	pH	DOC	Chl	DO	Hg	$\delta^{202}Hg$	$\Delta^{199}Hg$	$\Delta^{200}Hg$	$\Delta^{201}Hg$	$\Delta^{204}Hg$	$\delta^{202}Hg$	$\Delta^{199}Hg$	$\Delta^{200}Hg$	$\Delta^{201}Hg$	$\Delta^{204}Hg$
		m	℃		mg L^{-1}	ug L^{-1}	mg L^{-1}	ng L^{-1}	‰	‰	‰	‰	‰	2SD	2SD	2SD	2SD	2SD
Winter	N-DHg	0	15.1	8.66	4.12		12.1	2.15	-1.06	0.14	0.04	0.09	-0.09	0.07	0.06	0.05	0.07	0.12
	N-DHg	2	14.6	8.67	3.85		12.3	1.23	-0.91	0.08	0.14	0.01	-0.10	0.07	0.06	0.05	0.07	0.12
	N-DHg	4	12.8	8.74	3.94		12.2	1.89	-1.04	0.19	0.04	0.09	-0.03	0.07	0.06	0.05	0.07	0.12
	N-DHg	6	11.5	8.74	3.73		12.4	0.98	-0.83	0.18	0.14	0.11	0.01	0.09	0.06	0.05	0.12	0.12
	N-DHg	8	10.6	8.67	3.45		11.5	1.25	-0.63	0.13	0.04	0.09	-0.10	0.07	0.06	0.05	0.07	0.12
	N-DHg	10	9.8	8.64	3.12		7.44	0.87	-0.59	0.18	0.09	0.13	0.09	0.07	0.06	0.07	0.07	0.12
	N-DHg	14	8.4	8.57	2.68		5.1	0.98	-1.21	0.13	0.04	0.19	-0.02	0.07	0.06	0.07	0.07	0.12
	N-DHg	16	8.2	8.54	2.64		4.1	0.94	-0.80	0.28	0.02	0.08	-0.20	0.07	0.06	0.05	0.07	0.12
	N-DHg	20	7.6	8.48	2.26		3.8	0.78	-1.02	0.15	-0.01	0.17	0.00	0.07	0.06	0.05	0.07	0.12
	N-DHg	24	6.8	8.52	1.98		3.6	0.61	-0.11	0.06	-0.01	0.08	0.00	0.07	0.06	0.05	0.07	0.12
	N-DHg	28	5.9	8.53	1.56		3.2	0.48	-0.87	0.14	0.01	0.11	-0.04	0.07	0.07	0.09	0.07	0.12
	S-DHg	0	12.65	8.89	2.89		13.2	1.56	-0.56	0.17	0.11	0.12	-0.13	0.07	0.06	0.05	0.07	0.12
	S-DHg	2	10.65	8.88	3.12		12.5	1.45	-0.59	0.06	0.10	0.03	-0.15	0.07	0.06	0.05	0.07	0.12
	S-DHg	4	9.56	8.87	3.42		11.9	1.64	-0.70	0.25	0.10	0.16	0.06	0.07	0.06	0.05	0.07	0.12
	S-DHg	6	8.21	8.67	3.55		12.1	1.26	-0.94	0.18	0.03	0.07	-0.08	0.09	0.06	0.05	0.10	0.12
	S-DHg	8	6.55	8.64	4.12		11.5	1.12	-1.46	0.14	0.03	0.17	-0.08	0.09	0.06	0.05	0.10	0.12
	S-DHg	10	6.01	8.75	3.58		7.6	1.32	-1.31	0.14	0.06	0.10	0.01	0.07	0.06	0.05	0.07	0.20
	S-DHg	14	5.22	8.72	3.65		4.6	0.95	0.33	0.11	0.06	0.14	-0.15	0.07	0.12	0.10	0.02	0.13
	S-DHg	16	4.62	8.64	1.12		3.1	0.99	-0.86	0.23	0.00	0.19	-0.04	0.07	0.06	0.05	0.03	0.13
	S-DHg	20	4.32	8.65	1.68		2.1	0.56	-1.09	0.18	0.01	0.11	-0.02	0.07	0.06	0.05	0.03	0.13
Spring	N-DHg	0	23.21	8.88	4.15	2.59	10.01	2.34	-0.79	0.20	0.02	0.19	-0.19	0.07	0.06	0.05	0.07	0.12
	N-DHg	2	23.17	8.88	4.23	5.67	10.07	2.30	-1.55	0.40	0.08	0.31	-0.05	0.07	0.06	0.05	0.07	0.12
	N-DHg	4	22.90	8.87	3.89	8.57	10.33	1.73	-2.11	0.34	0.11	0.14	-0.21	0.07	0.06	0.05	0.07	0.12
	N-DHg	6	20.22	8.30	3.63	10.96	10.02	1.44	-1.21	0.28	0.10	0.19	-0.08	0.07	0.08	0.05	0.08	0.26
	N-DHg	8	16.51	8.78	3.26	9.25	9.49	1.82	-0.96	0.28	0.01	0.33	0.11	0.07	0.11	0.05	0.07	0.12
	N-DHg	10	14.77	8.76	3.12	3.63	6.89	2.15	-1.14	0.25	0.01	0.12	0.01	0.07	0.06	0.05	0.07	0.12
	N-DHg	14	13.45	8.91	2.98	0.83	5.46	1.73	-2.26	0.18	0.01	0.11	-0.02	0.07	0.06	0.05	0.07	0.12
	N-DHg	16	12.48	8.82	2.75	0.36	3.79	0.64	-1.75	0.24	0.01	0.17	-0.53	0.12	0.06	0.05	0.10	0.16
	N-DHg	20	11.80	8.69	2.64	-0.05	3.37	1.20	-0.79	0.26	0.05	0.26	0.10	0.07	0.11	0.05	0.07	0.12
	N-DHg	24	11.40	8.66	2.31	-0.38	3.10	0.88	-0.97	0.28	-0.02	0.22	0.03	0.12	0.06	0.05	0.10	0.16

	S-DHg	0	23.88	9.25	4.86	11.31	11.97	2.45	-1.34	0.56	0.07	0.26	-0.07	0.12	0.13	0.05	0.07	0.27
	S-DHg	2	23.70	9.24	4.75	20.65	12.04	2.27	-1.07	0.24	0.08	0.22	-0.10	0.07	0.06	0.06	0.07	0.17
	S-DHg	4	23.29	9.22	4.62	13.28	11.05	1.80	-0.97	0.32	0.07	0.30	0.03	0.07	0.06	0.06	0.07	0.17
	S-DHg	6	16.00	8.98	3.82	3.56	6.38	1.63	-1.35	0.35	-0.01	0.31	-0.04	0.07	0.06	0.06	0.17	0.16
	S-DHg	10	15.20	8.90	3.58	2.59	1.91	2.62	-0.92	0.52	-0.01	0.32	-0.17	0.07	0.06	0.05	0.07	0.12
	S-DHg	14	13.14	8.70	3.35	1.48	0.40	1.62	-1.14	0.38	0.08	0.22	0.03	0.12	0.13	0.05	0.07	0.27
	S-DHg	16	12.35	8.60	2.98	0.85	0.29	1.04	-1.08	0.12	-0.01	0.02	0.00	0.07	0.06	0.05	0.07	0.12
	S-DHg	20	12.05	8.57	3.12	0.91	0.27	1.68	-1.56	0.07	0.03	0.04	-0.08	0.07	0.06	0.05	0.07	0.12
Summer	N-DHg	0	25.06	8.51	4.23	7.51	6.11	2.10	-0.84	0.04	0.03	0.03	-0.08	0.07	0.06	0.05	0.07	0.12
	N-DHg	2	25.07	8.55	3.89	8.74	6.02	1.93	-0.36	0.03	0.03	0.01	-0.11	0.07	0.06	0.05	0.07	0.12
	N-DHg	4	25.06	8.57	3.56	8.93	5.99	1.90	-0.59	0.19	0.03	0.07	-0.09	0.12	0.06	0.05	0.07	0.12
	N-DHg	6	25.06	8.59	3.58	8.45	5.87	1.85	-0.42	0.15	0.00	0.20	-0.12	0.07	0.06	0.05	0.07	0.12
	N-DHg	8	25.06	8.60	3.00	8.49	5.79	2.08	-0.40	0.16	0.00	0.15	-0.11	0.12	0.06	0.05	0.07	0.12
	N-DHg	10	25.06	8.60	3.05	8.55	5.77	1.17	-0.82	0.11	0.04	0.12	-0.01	0.07	0.06	0.05	0.07	0.12
	N-DHg	12	24.88	8.59	3.15	1.02	3.15	1.31	-0.34	0.19	0.01	0.25	-0.02	0.08	0.06	0.05	0.07	0.12
	N-DHg	14	23.97	8.45	3.01	0.08	0.93	1.69	-0.70	0.15	0.02	0.20	-0.02	0.11	0.06	0.05	0.07	0.13
	N-DHg	16	23.51	8.42	2.98	0.00	0.71	1.24	-0.71	0.08	0.01	0.11	-0.01	0.08	0.06	0.05	0.07	0.12
	N-DHg	18	23.14	8.39	2.64	0.00	0.49	1.30	-0.89	0.13	-0.02	0.13	-0.08	0.11	0.06	0.05	0.07	0.13
	N-DHg	20	22.85	8.34	2.58	0.01	0.38	0.93	-0.70	0.13	0.00	0.11	-0.13	0.12	0.06	0.05	0.07	0.12
	N-DHg	24	22.70	8.28	2.48	0.17	0.33	1.34	-0.80	0.13	0.06	0.15	-0.08	0.12	0.06	0.05	0.07	0.12
	N-DHg	28	22.41	8.18	2.24	0.07	0.27	1.82	-0.70	0.11	-0.01	0.17	-0.04	0.07	0.06	0.05	0.07	0.12
	S-DHg	0	24.54	8.5	4.58	6.26	6.99	2.56	-0.90	0.20	0.05	0.09	-0.08	0.11	0.06	0.05	0.09	0.12
	S-DHg	2	24.55	8.52	4.35	8.08	6.91	2.58	-0.63	0.21	0.06	0.05	-0.09	0.11	0.06	0.05	0.09	0.12
	S-DHg	4	24.55	8.54	3.98	8.47	6.87	1.91	-0.70	0.12	0.05	0.04	-0.04	0.07	0.10	0.07	0.07	0.12
	S-DHg	6	24.54	8.55	3.84	8.58	6.81	1.96	-0.66	0.13	0.05	0.18	-0.04	0.07	0.23	0.05	0.07	0.12
	S-DHg	8	24.53	8.56	3.56	8.50	6.75	1.15	-0.90	0.17	0.06	0.18	0.39	0.11	0.13	0.07	0.07	0.13
	S-DHg	10	24.50	8.57	3.42	8.71	6.69	1.29	-0.66	0.10	0.00	0.13	0.29	0.11	0.13	0.07	0.07	0.13
	S-DHg	14	24.46	8.59	3.15	8.71	6.25	1.99	-0.37	0.17	0.04	0.10	-0.01	0.07	0.23	0.05	0.07	0.12
	S-DHg	16	23.03	8.59	2.87	0.53	2.89	0.63	-0.51	0.19	0.02	0.19	-0.02	0.12	0.06	0.05	0.07	0.12
	S-DHg	18	22.97	8.43	2.32	0.60	1.11	0.54	-0.46	0.14	0.01	0.20	-0.04	0.07	0.06	0.05	0.07	0.12

Table S9. Concentrations and isotope compositions of particulate Hg (PHg) in vertical profile at HFL. HFL-N and HFL-S represent the sampling site of northern and southern catchment area, respectively, of Hongfeng lake.

Time	Sample ID	Depth	Hg	Tem	PH	DOC	DO	Chl	SPM	Log K_d	$\delta^{202}Hg$	$\Delta^{199}Hg$	$\Delta^{200}Hg$	$\Delta^{201}Hg$	$\Delta^{204}Hg$	$\delta^{202}Hg$	$\Delta^{199}Hg$	$\Delta^{200}Hg$	$\Delta^{201}Hg$	$\Delta^{204}Hg$
		m	ng L^{-1}	℃		mg L^{-1}	mg L^{-1}	ug L^{-1}	mg L^{-1}		‰	‰	‰	‰	‰	2SD	2SD	2SD	2SD	2SD
Winter	N-PHg	0	3.89	15.10	8.66	4.12	12.10		10.59	5.23	-1.31	-0.02	-0.03	-0.02	0.14	0.11	0.06	0.05	0.07	0.12
	N-PHg	2	3.00	14.60	8.67	3.85	12.30		8.95	5.44	-1.31	-0.02	-0.03	-0.05	0.15	0.07	0.08	0.05	0.16	0.12
	N-PHg	4	2.97	12.80	8.74	3.94	12.20		9.06	5.24	-1.44	0.02	-0.01	0.02	-0.15	0.07	0.08	0.05	0.16	0.12
	N-PHg	6	2.98	11.50	8.74	3.73	12.40		8.25	5.57	-1.37	-0.05	0.01	-0.04	-0.03	0.07	0.06	0.05	0.07	0.16
	N-PHg	8	2.90	10.60	8.67	3.45	11.50		9.58	5.39	-0.90	-0.03	0.03	-0.01	0.03	0.12	0.06	0.05	0.10	0.16
	N-PHg	10	2.43	9.80	8.64	3.12	7.44		8.80	5.50	-1.49	0.02	0.00	-0.05	-0.01	0.11	0.06	0.05	0.07	0.12
	N-PHg	14	2.51	8.40	8.57	2.68	5.10		8.50	5.48	-1.54	-0.03	-0.03	-0.04	-0.06	0.07	0.06	0.05	0.07	0.12
	N-PHg	16	2.38	8.20	8.54	2.64	4.10		8.47	5.48	-1.49	-0.03	-0.05	-0.03	0.04	0.07	0.06	0.05	0.07	0.12
	N-PHg	20	2.04	7.60	8.48	2.26	3.80		7.36	5.55	-1.52	0.03	-0.01	-0.01	0.02	0.07	0.06	0.05	0.07	0.12
	N-PHg	24	2.83	6.80	8.52	1.98	3.60		7.37	5.80	-1.65	-0.04	-0.05	-0.06	0.01	0.07	0.06	0.05	0.07	0.12
	N-PHg	28	2.62	5.90	8.53	1.56	3.20		7.03	5.89	-0.78	-0.04	-0.01	-0.05	0.02	0.07	0.11	0.05	0.07	0.12
	S-PHg	0	4.24	12.65	8.89	2.89	13.20		11.62	5.37	-1.35	-0.10	0.01	-0.14	-0.06	0.07	0.06	0.05	0.07	0.12
	S-PHg	2	3.96	10.65	8.88	3.12	12.50		10.09	5.43	-2.66	-0.12	0.01	-0.13	-0.19	0.09	0.06	0.05	0.07	0.12
	S-PHg	4	3.17	9.56	8.87	3.42	11.90		8.22	5.37	-1.74	-0.09	0.04	-0.13	-0.12	0.07	0.06	0.05	0.07	0.12
	S-PHg	6	3.88	8.21	8.67	3.55	12.10		8.52	5.51	-1.34	-0.14	0.00	-0.16	-0.03	0.07	0.06	0.05	0.07	0.12
	S-PHg	8	3.36	6.55	8.64	4.12	11.50		8.09	5.57	-1.43	-0.08	0.03	-0.08	-0.12	0.07	0.06	0.06	0.07	0.12
	S-PHg	10	3.68	6.01	8.75	3.58	7.60		9.03	5.49	-1.56	-0.07	-0.02	-0.08	-0.10	0.07	0.06	0.05	0.07	0.12
	S-PHg	14	3.19	5.22	8.72	3.65	4.60		7.58	5.64	-2.03	-0.10	-0.01	-0.16	-0.08	0.07	0.06	0.05	0.07	0.12
	S-PHg	16	3.15	4.62	8.64	4.12	3.12		7.73	5.62	0.12	-0.02	-0.02	-0.02	-0.04	0.07	0.06	0.05	0.07	0.12
	S-PHg	20	3.23	4.32	8.65	3.68	2.14		7.10	5.91	-1.87	-0.03	0.03	-0.05	-0.16	0.07	0.09	0.05	0.07	0.12
Spring	N-PHg	0	3.38	23.21	8.88	4.15	10.01	2.59	8.96	5.21	-1.55	-0.01	0.00	-0.02	0.07	0.07	0.06	0.06	0.07	0.12
	N-PHg	2	2.97	23.17	8.88	4.23	10.07	5.67	10.29	5.10	-1.80	-0.06	-0.01	-0.01	-0.04	0.10	0.06	0.06	0.08	0.12
	N-PHg	4	3.47	22.90	8.87	3.89	10.33	8.57	10.01	5.30	-1.40	0.01	0.00	-0.02	-0.07	0.07	0.06	0.06	0.07	0.12
	N-PHg	6	4.18	20.22	8.30	3.63	10.02	10.96	10.60	5.44	-2.24	-0.01	-0.02	-0.05	-0.20	0.07	0.06	0.06	0.07	0.12
	N-PHg	8	3.20	16.51	8.78	3.26	9.49	9.25	8.97	5.29	-2.25	0.00	-0.01	0.01	-0.02	0.07	0.06	0.06	0.17	0.16
	N-PHg	10	3.92	14.77	8.76	3.12	6.89	3.63	9.57	5.28	-2.44	-0.06	0.00	-0.03	-0.20	0.07	0.06	0.06	0.17	0.16
	N-PHg	14	3.25	13.45	8.91	2.98	5.46	0.83	8.80	5.33	-2.02	0.01	-0.02	0.05	-0.27	0.07	0.06	0.06	0.07	0.12
	N-PHg	16	3.17	12.48	8.82	2.75	3.79	0.36	9.12	5.73	-1.55	-0.07	0.00	-0.03	0.07	0.07	0.09	0.05	0.07	0.12
	N-PHg	20	2.34	11.80	8.69	2.64	3.37	-0.05	6.00	5.51	-1.81	-0.04	-0.02	-0.04	-0.16	0.07	0.06	0.06	0.07	0.12
	N-PHg	24	1.87	11.40	8.66	2.31	3.10	-0.38	7.16	5.47	-1.44	-0.07	-0.03	-0.09	0.27	0.07	0.06	0.12	0.07	0.12
	N-PHg	28	1.91	11.23	8.52	2.14	3.00	-0.50			-2.20	-0.10	-0.04	-0.06	-0.01	0.10	0.07	0.14	0.07	0.12

	S-PHg	0	5.17	23.88	9.25	4.86	11.97	11.31	8.13	5.41	-1.32	-0.03	-0.02	-0.04	-0.06	0.07	0.06	0.05	0.07	0.16
	S-PHg	2	3.96	23.70	9.24	4.75	12.04	20.65	9.60	5.26	-1.33	0.02	0.00	0.00	-0.19	0.07	0.06	0.06	0.17	0.16
	S-PHg	4	2.71	23.29	9.22	4.62	11.05	13.28	8.18	5.27	-2.17	-0.03	-0.01	-0.04	0.07	0.09	0.06	0.05	0.07	0.12
	S-PHg	6	3.47	19.97	9.15	4.37	6.38	8.20	7.80	5.44	-2.44	-0.11	-0.01	0.02	-0.25	0.12	0.13	0.05	0.07	0.27
	S-PHg	10	2.32	15.20	8.90	3.58	1.91	2.59	5.13	5.24	-1.65	-0.04	-0.04	-0.04	-0.11	0.07	0.06	0.06	0.07	0.12
	S-PHg	14	2.51	13.14	8.70	3.35	0.40	1.48	6.82	5.36	-1.36	-0.04	0.04	-0.03	0.14	0.07	0.06	0.05	0.07	0.12
	S-PHg	16	2.24	12.35	8.60	2.98	0.29	0.85	5.87	5.56	-1.35	-0.06	-0.01	-0.08	0.12	0.07	0.06	0.05	0.10	0.12
	S-PHg	20	2.54	12.05	8.57	3.12	0.27	0.91	5.04	5.48	-1.82	-0.07	0.00	-0.07	-0.14	0.10	0.10	0.05	0.07	0.12
Summer	N-PHg	0	3.71	25.06	8.51	4.23	6.11	7.51	10.50	5.23	-1.44	-0.03	-0.03	-0.02	-0.06	0.10	0.07	0.06	0.07	0.12
	N-PHg	2	3.05	25.07	8.55	3.89	6.02	8.74	8.78	5.26	-1.16	-0.06	-0.02	-0.05	-0.16	0.07	0.06	0.05	0.07	0.12
	N-PHg	4	3.38	25.06	8.57	3.56	5.99	8.93	8.02	5.35	-1.25	-0.06	-0.01	-0.05	-0.07	0.10	0.10	0.05	0.07	0.12
	N-PHg	6	2.89	25.06	8.59	3.58	5.87	8.45	8.17	5.28	-1.20	-0.05	-0.03	-0.03	-0.01	0.07	0.06	0.08	0.07	0.12
	N-PHg	8	2.28	25.06	8.60	3.00	5.79	8.49	5.99	5.26	-1.57	-0.03	-0.05	-0.06	-0.13	0.07	0.06	0.12	0.07	0.12
	N-PHg	10	3.27	25.06	8.60	3.05	5.77	8.55	8.21	5.53	-1.55	0.05	0.04	0.05	0.07	0.07	0.06	0.05	0.07	0.12
	N-PHg	12	2.07	24.88	8.59	3.15	3.15	1.02	6.30	5.40	-1.28	-0.05	0.01	-0.02	0.10	0.07	0.06	0.05	0.07	0.12
	N-PHg	14	2.38	23.97	8.45	3.01	0.93	0.08	5.95	5.31	-1.18	-0.07	0.00	-0.07	-0.12	0.08	0.06	0.05	0.07	0.12
	N-PHg	16	1.72	23.51	8.42	2.98	0.71	-0.04	7.10	5.29	-1.15	-0.02	-0.04	-0.02	0.23	0.10	0.10	0.05	0.07	0.12
	N-PHg	18	1.92	23.14	8.39	2.64	0.49	0.00	6.46	5.36	-1.40	-0.01	0.01	-0.01	-0.10	0.08	0.06	0.05	0.07	0.12
	N-PHg	20	1.72	22.85	8.34	2.58	0.38	0.01	6.73	5.44	-1.27	-0.02	-0.06	-0.01	-0.27	0.07	0.06	0.08	0.07	0.12
	N-PHg	24	1.62	22.70	8.28	2.48	0.33	0.17	6.75	5.25	-1.55	-0.03	0.01	0.00	-0.06	0.07	0.06	0.05	0.07	0.12
	N-PHg	28	2.17	22.41	8.18	2.24	0.27	0.07	5.27	5.36	-1.63	-0.02	-0.02	-0.03	-0.01	0.08	0.06	0.05	0.07	0.12
	S-PHg	0	3.30	24.54	8.50	4.58	6.99	6.26	9.39	5.14	-1.14	-0.14	-0.04	-0.15	0.07	0.08	0.06	0.05	0.07	0.12
	S-PHg	2	3.43	24.55	8.52	4.35	6.91	8.08	9.36	5.15	-1.65	-0.07	0.00	-0.10	0.06	0.08	0.06	0.05	0.07	0.12
	S-PHg	4	3.06	24.55	8.54	3.98	6.87	8.47	7.60	5.32	-1.61	-0.05	-0.01	-0.11	-0.02	0.07	0.06	0.05	0.08	0.12
	S-PHg	6	2.93	24.54	8.55	3.84	6.81	8.58	9.85	5.18	-1.78	-0.11	-0.03	-0.12	0.11	0.07	0.07	0.05	0.07	0.12
	S-PHg	8	2.87	24.53	8.56	3.56	6.75	8.50	7.19	5.54	-1.58	-0.08	-0.05	-0.06	0.16	0.07	0.07	0.05	0.07	0.12
	S-PHg	10	3.00	24.50	8.57	3.42	6.69	8.71	7.95	5.47	-1.54	-0.17	-0.02	-0.22	0.09	0.07	0.06	0.05	0.07	0.12
	S-PHg	12	2.66	24.48	8.58	3.21	6.62	8.77			-1.53	-0.15	-0.01	-0.21	0.06	0.07	0.07	0.05	0.07	0.12
	S-PHg	14	2.98	24.46	8.59	3.15	6.25	8.71	5.93	5.40	-1.53	-0.17	-0.05	-0.17	0.03	0.07	0.07	0.05	0.07	0.12
	S-PHg	16	2.65	23.03	8.59	2.87	2.89	0.53	5.94	5.85	-1.72	-0.02	-0.04	-0.11	-0.12	0.12	0.06	0.05	0.10	0.16
	S-PHg	18	2.86	22.97	8.43	2.32	1.11	0.60	5.75	5.96	-1.81	-0.07	-0.05	-0.15	0.00	0.08	0.06	0.05	0.07	0.12

Table S10. Hg concentration and isotope compositions of sediments in HFL.

Sample ID	Hg conc	$\delta^{202}Hg$	$\Delta^{199}Hg$	$\Delta^{200}Hg$	$\Delta^{201}Hg$	$\Delta^{204}Hg$	$\delta^{202}Hg$	$\Delta^{199}Hg$	$\Delta^{200}Hg$	$\Delta^{201}Hg$	$\Delta^{204}Hg$
	ng g^{-1}	‰	‰	‰	‰	‰	2SD	2SD	2SD	2SD	2SD
Sediment-1	511.03	-1.54	-0.13	-0.03	-0.09	0.09	0.07	0.06	0.07	0.07	0.14
Sediment-2	484.53	-1.60	-0.08	-0.04	-0.13	0.16	0.07	0.06	0.07	0.07	0.14
Sediment-3	464.60	-1.68	-0.05	-0.03	-0.12	0.14	0.07	0.06	0.07	0.07	0.14
Sediment-4	447.83	-1.47	-0.08	-0.04	-0.14	-0.05	0.07	0.07	0.07	0.09	0.12
Sediment-5	459.39	-1.59	-0.07	-0.04	-0.16	0.11	0.07	0.07	0.07	0.09	0.12
Sediment-6	442.87	-1.76	-0.09	-0.04	-0.07	0.02	0.07	0.07	0.07	0.09	0.12
Sediment-7	508.88	-1.77	-0.09	-0.04	-0.08	0.00	0.07	0.07	0.07	0.09	0.12

Table S11. The chronology in sediment core of HFL. Note that HFL Reservoir was constructed in 1960.

Sample ID	Depth	Mass depth	Age
	cm	g cm^{-2}	AD
HFL-1	1	0.06	2021
HFL-2	2	0.17	2021
HFL-3	3	0.26	2021
HFL-4	4	0.36	2020
HFL-5	5	0.49	2020
HFL-6	6	0.60	2019
HFL-7	7	0.70	2018
HFL-8	8	0.82	2018
HFL-9	9	0.95	2017
HFL-10	10	1.12	2016
HFL-11	11	1.28	2015
HFL-12	12	1.46	2014
HFL-13	13	1.64	2013
HFL-14	14	1.82	2012
HFL-15	15	2.01	2011
HFL-16	16	2.16	2011
HFL-17	17	2.34	2010
HFL-18	18	2.53	2009
HFL-19	19	2.75	2007
HFL-20	20	2.94	2006
HFL-21	21	3.12	2005
HFL-22	22	3.32	2004
HFL-23	23	3.47	2004
HFL-24	24	3.64	2003
HFL-25	25	3.86	2001
HFL-26	26	4.08	2000
HFL-27	27	4.31	1999
HFL-28	28	4.54	1998
HFL-29	29	4.79	1996
HFL-30	30	5.05	1995
HFL-31	31	5.30	1994
HFL-32	32	5.53	1993
HFL-33	33	5.83	1991
HFL-34	34	6.22	1989
HFL-35	35	6.68	1986
HFL-36	36	7.16	1984
HFL-37	37	7.66	1981
HFL-38	38	8.19	1978
HFL-39	39	8.71	1975
HFL-40	40	9.30	1972
HFL-41	41	9.86	1969
HFL-42	42	10.37	1967
HFL-43	43	10.93	1964
HFL-44	44	11.41	1961

Reference:

1. Araujo, B.F., Osterwalder, S., Szponar, N., Lee, D., Petrova, M.V., Pernov, J.B., Ahmed, S., Heimburger-Boavida, L.E., Laffont, L., Teisserenc, R., Tananaev, N., Nordstrom, C., Magand, O., Stupple, G., Skov, H., Steffen, A., Bergquist, B., Pfaffhuber, K.A., Thomas, J.L., Scheper, S., Petaja, T., Dommergue, A. and Sonke, J.E. (2022) Mercury isotope evidence for Arctic summertime re-emission of mercury from the cryosphere. Nature Communications 13(1), 4956.

2. Engstrom, D.R. (2007) Fish respond when the mercury rises. Proceedings of the National Academy of Sciences of the United States of America 104(42), 16394-16395.

3. Fu, X.W., Heimburger, L.E. and Sonke, J.E. (2014) Collection of atmospheric gaseous mercury for stable isotope analysis using iodine- and chlorine-impregnated activated carbon traps. Journal of Analytical Atomic Spectrometry 29(5), 841-852.

4. Fu, X.W., Yang, X., Lang, X.F., Zhou, J., Zhang, H., Yu, B., Yan, H.Y., Lin, C.J. and Feng, X.B. (2016) Atmospheric wet and litterfall mercury deposition at urban and rural sites in China. Atmospheric Chemistry and Physics 16(18), 11547-11562.

5. Jiskra, M., Wiederhold, J.G., Bourdon, B. and Kretzschmar, R. (2012) Solution Speciation Controls Mercury Isotope Fractionation of Hg(II) Sorption to Goethite. Environmental Science & Technology 46(12), 6654-6662.

6. Lee, H.S., Hur, J., Lee, M.H., Brogi, S.R., Kim, T.W. and Shin, H.S. (2019) Photochemical release of dissolved organic matter from particulate organic matter: Spectroscopic characteristics and disinfection by-product formation potential. Chemosphere 235, 586-595.

7. Wiederhold, J.G., Cramer, C.J., Daniel, K., Infante, I., Bourdon, B. and Kretzschmar, R. (2010) Equilibrium Mercury Isotope Fractionation between Dissolved Hg(II) Species and Thiol-Bound Hg. Environmental Science & Technology 44(11), 4191-4197.

8. Wu, X., Fu, X.W., Zhang, H., Tang, K.H., Wang, X., Zhang, H., Deng, Q.W., Zhang, L.M., Liu, K.Y., Wu, Q.R., Wang, S.X. and Feng, X.B. (2023) Changes in Atmospheric Gaseous Elemental Mercury Concentrations and Isotopic Compositions at Mt. Changbai During 2015-2021 and Mt. Ailao During 2017-2021 in China. Journal of Geophysical Research-Atmospheres 128(10), e2022JD037749.

9. Zhang, H., Fu, X.W., Wu, X., Deng, Q.W., Tang, K.H., Zhang, L.M., Sommar, J., Sun, G.Y. and Feng, X.B. (2023) Using Mercury Stable Isotopes to Quantify Bidirectional Water-Atmosphere Hg(0) Exchange Fluxes and Explore Controlling Factors. Environmental Science & Technology 57(29), 10673-10685.